

Unified Entrainment and Detrainment Closures for Extended Eddy-Diffusivity Mass-Flux Schemes

Cohen Yair¹, Lopez-Gomez Ignacio¹, Jaruga Anna², He Jia¹, Kaul Colleen³, and Schneider Tapio²

¹California Institute of Technology

²Jet Propulsion Laboratory, California Institute of Technology

³Pacific Northwest National Laboratory

November 16, 2022

Abstract

We demonstrate that an extended eddy-diffusivity mass-flux (EDMF) scheme can be used as a unified parameterization of subgrid-scale turbulence and convection across a range of dynamical regimes, from dry convective boundary layers, over shallow convection, to deep convection. Central to achieving this unified representation of subgrid-scale motions are entrainment and detrainment closures. We model entrainment and detrainment rates as a combination of turbulent and dynamical processes. Turbulent entrainment/detrainment is represented as downgradient diffusion between plumes and their environment. Dynamical entrainment/detrainment are proportional to a ratio of buoyancy difference and vertical velocity scale, partitioned based on buoyancy sorting approaches and modulated by a function of relative humidity difference in cloud layer to represent buoyancy loss owing to evaporation in mixing. We first evaluate the closures offline against entrainment and detrainment rates diagnosed from large-eddy simulations (LES) in which tracers are used to identify plumes, their turbulent environment, and mass and tracer exchanges between them. The LES are of canonical test cases of a dry convective boundary layer, shallow convection, and deep convection, thus spanning a broad range of regimes. We then compare the LES with the full EDMF scheme, including the new closures, in a single column model (SCM). The results show good agreement between the SCM and LES in quantities that are key for climate models, including thermodynamic profiles, cloud liquid water profiles, and profiles of higher moments of turbulent statistics. The SCM also captures well the diurnal cycle of convection and the onset of precipitation.

Unified Entrainment and Detrainment Closures for Extended Eddy-Diffusivity Mass-Flux Schemes

Yair Cohen¹, Ignacio Lopez-Gomez¹, Anna Jaruga^{1,2}, Jia He¹, Colleen Kaul³,
Tapio Schneider^{1,2}

¹California Institute of Technology, Pasadena, California, USA.

²Jet Propulsion Laboratory, California Institute of Technology, Pasadena, California, USA.

³Pacific Northwest National Laboratory, Washington, USA

Key Points:

- An extended eddy-diffusivity mass-flux (EDMF) scheme successfully captures diverse regimes of convective motions.
- Unified closures are presented for entrainment and detrainment across the different convective regimes.
- With the unified closures, the EDMF scheme can simulate dry convection, shallow cumulus, and deep cumulus.

Corresponding author: Tapio Schneider, tapio@caltech.edu

Abstract

We demonstrate that an extended eddy-diffusivity mass-flux (EDMF) scheme can be used as a unified parameterization of subgrid-scale turbulence and convection across a range of dynamical regimes, from dry convective boundary layers, over shallow convection, to deep convection. Central to achieving this unified representation of subgrid-scale motions are entrainment and detrainment closures. We model entrainment and detrainment rates as a combination of turbulent and dynamical processes. Turbulent entrainment/detrainment is represented as downgradient diffusion between plumes and their environment. Dynamical entrainment/detrainment are proportional to a ratio of buoyancy difference and vertical velocity scale, partitioned based on buoyancy sorting approaches and modulated by a function of relative humidity difference in cloud layer to represent buoyancy loss owing to evaporation in mixing. We first evaluate the closures offline against entrainment and detrainment rates diagnosed from large-eddy simulations (LES) in which tracers are used to identify plumes, their turbulent environment, and mass and tracer exchanges between them. The LES are of canonical test cases of a dry convective boundary layer, shallow convection, and deep convection, thus spanning a broad range of regimes. We then compare the LES with the full EDMF scheme, including the new closures, in a single column model (SCM). The results show good agreement between the SCM and LES in quantities that are key for climate models, including thermodynamic profiles, cloud liquid water profiles, and profiles of higher moments of turbulent statistics. The SCM also captures well the diurnal cycle of convection and the onset of precipitation.

Plain Language Summary

The dynamics of clouds and their underlying turbulence are too small in scale to be resolved in global models of the atmosphere, yet they play a crucial role controlling weather and climate. Climate and weather forecasting models rely on parameterizations to represent the dynamics of clouds and turbulence. Inadequacies in these parameterizations have hampered especially climate models for decades; they are the largest source of physical uncertainties in climate predictions. It has proven challenging to represent the wide range of cloud and turbulence regimes encountered in nature in a parameterization that can capture them in a unified physical framework. Here we present a parameterization that does capture a wide range of cloud and turbulence regimes within a single, unified physical framework, with relatively few parameters that can be adjusted to fit data. The framework relies on a decomposition of turbulent flows into coherent up- and downdrafts (i.e. plumes) and random turbulence in their environment. A key contribution of this paper is to show how the interaction between the plumes and their turbulent environment—the so-called entrainment and detrainment of air into and out of plumes—can be modeled. We show that the resulting parameterization represents well the most important features of dry convective boundary layers, shallow cumulus convection, and deep cumulonimbus convection.

1 Introduction

Turbulence and convection play an important role in the climate system. They transport energy, moisture, and momentum vertically, thereby controlling the formation of clouds and, especially in the tropics, the thermal stratification of the atmosphere. They occur on a wide range of scales, from motions on scales of meters to tens of meters in stable boundary layers and near the trade inversion, to motions on scales of kilometers in deep convection. General Circulation Models (GCMs), with horizontal resolutions approaching tens of kilometers, are unable to resolve this spectrum of motions. Turbulence and convection will remain unresolvable in GCMs for the foreseeable future (Schneider et al., 2017), although some deep-convective motions, on scales of kilometers to tens of

64 kilometers, are beginning to be resolved in short-term global simulations (Kajikawa et
65 al., 2016; Stevens et al., 2019).

66 Unable to resolve turbulence and convection explicitly, GCMs rely on parameter-
67 ization schemes to represent subgrid-scale (SGS) motions. Typically, GCMs have sev-
68 eral distinct parameterization schemes for representing, for example, boundary layer tur-
69 bulence, stratocumulus clouds, shallow convection, and deep convection. The different
70 parameterization schemes interact via trigger functions with discontinuous behavior in
71 parameter space, even though in reality the flow regimes they represent lie on a contin-
72 uous spectrum, (Xie et al., 2019). This fragmentary representation of SGS motion by
73 multiple schemes leads to a proliferation of adjustable parameters, including paramet-
74 ric triggering functions that switch between schemes. Moreover, most existing param-
75 eterizations rely on statistical equilibrium assumptions between the SGS motions and
76 the resolved scales. These assumptions become invalid as model resolution increases and,
77 for example, some aspects of deep convection begin to be explicitly resolved (Dirmeyer
78 et al., 2012; Gao et al., 2017). It is widely recognized that these issues make model cal-
79 ibration challenging and compromise our ability to make reliable climate predictions (Hourdin
80 et al., 2017; Schmidt et al., 2017; Schneider et al., 2017).

81 Many known biases in climate models and uncertainties in climate predictions are
82 attributed to difficulties in representing SGS turbulence and convection. For example,
83 biases in the diurnal cycle and the continental near-surface temperature, especially in
84 polar regions, have been traced to inadequacies in turbulence parameterizations for sta-
85 ble boundary layers (Holtslag et al., 2013). Across climate models, biases in how trop-
86 ical cloud cover co-varies with temperature and other environmental factors on seasonal
87 and interannual timescales are correlated with the equilibrium climate sensitivity, thus
88 revealing the important role the representation of tropical low clouds plays in uncertain-
89 ties in climate predictions (Bony & Dufresne, 2005; Teixeira et al., 2011; Nam et al., 2012;
90 Lin et al., 2014; Brient et al., 2016; Brient & Schneider, 2016; Ceppi et al., 2017; Cesana
91 et al., n.d.; Caldwell et al., 2018; Dong et al., 2019; Schneider et al., 2019). Differences
92 in moisture export from the mixed layer to the free troposphere by cumulus convection
93 lead to differences in the width and strength of the ascending branch of the Hadley cir-
94 culation (R. A. Neggers et al., 2007). And biases in the structure of the South Pacific
95 Convergence Zone have been traced to biases in the intensity of deep-convective updrafts
96 (Hirota et al., 2014). It is evident from these few examples that progress in the repre-
97 sentation of SGS turbulence and convection is crucial for progress in climate modeling
98 and prediction. At the same time, it is desirable to unify the representation of SGS mo-
99 tions in one continuous parameterization scheme, to reduce the number of adjustable pa-
100 rameters and obtain a scheme that more faithfully represents the underlying continuum
101 of physical processes.

102 Different approaches for a systematic coarse graining of the equations of motion,
103 leading to a unified parameterization, have been proposed (Lappen & Randall, 2001a;
104 de Rooy & Siebesma, 2010; Yano, 2014; Park, 2014a, 2014b; Thuburn et al., 2018; Tan
105 et al., 2018; Han & Bretherton, 2019; Rio et al., 2019; Suselj et al., 2019b). They typ-
106 ically entail a conditional averaging (or filtering) of the governing equations over several
107 subdomains (Weller & McIntyre, 2019), or an assumed probability density function (PDF)
108 ansatz for dynamical variables and generation of moment equations from the ansatz (Lappen
109 & Randall, 2001a; Golaz et al., 2002; Larson & Golaz, 2005; Larson et al., 2012). For
110 example, conditional averaging can lead to a partitioning of a GCM grid box into sub-
111 domains representing coherent ascending and descending plumes, or drafts, and a more
112 isotropically turbulent environment. Unclosed terms arise that, for example, represent
113 interactions among subdomains through entrainment and detrainment. Such unclosed
114 terms need to be specified through closure assumptions (de Rooy et al., 2013). Or, if mo-
115 ment equations are generated through an assumed PDF ansatz for dynamical and ther-
116 modynamic variables, unclosed interactions among moments and dissipation terms need

117 to be specified through closure assumptions (Lappen & Randall, 2001b; Golaz et al., 2002).
 118 Our goal in this paper is to develop a unified set of closures that work across the range
 119 of turbulent and convective motions, within one specific type of parameterization scheme
 120 known as an eddy diffusivity/mass flux (EDMF) scheme (A. P. Siebesma & Teixeira, 2000;
 121 A. P. Siebesma et al., 2007; Wu et al., 2020).

122 We build on the extended EDMF scheme of Tan et al. (2018), which extends the
 123 original EDMF parameterization A. P. Siebesma and Teixeira (2000) by retaining ex-
 124 plicit time dependence (SGS memory) and treating subdomain second-moment equations
 125 consistently, so that, for example, energy exchange between plumes and their environ-
 126 ment obeys conservation requirements. The explicit SGS memory avoids any statisti-
 127 cal equilibrium assumption and allows the scheme to operate in the convective gray zone,
 128 where deep convective motions begin to become resolved.

129 In this and a companion paper Lopez-Gomez et al. (2020), along with a revised pres-
 130 sure closure (Jia He, personal communication), we present a set of unified closures that
 131 allow the extended EDMF parameterization to simulate stable boundary layers, dry con-
 132 vective boundary layers, stratocumulus-topped boundary layers, shallow convection, and
 133 deep convection, all within a scheme with unified closures and a single set of param-
 134 eters. This paper focuses on unified entrainment and detrainment closures that are es-
 135 sential for convective regime, and Lopez-Gomez et al. (2020) presents a closure for tur-
 136 bulent mixing. To demonstrate the viability of our approach, we compare the resulting
 137 parameterization scheme against large-eddy simulations (LES) of several canonical test
 138 cases for different dynamical regimes.

139 This paper is organized as follows. In section 2, we present the general structure
 140 of the extended EDMF scheme, including the subdomain decomposition and the prog-
 141 nostic equations for subdomain moments. Section 3 introduces the entrainment and de-
 142 trainment closures that are key for the scheme to work across different dynamical regimes.
 143 Section 4 describes the numerical implementation of this scheme in a single column model
 144 (SCM). In section 5, we describe the LES used in this study and how we compare terms
 145 in the EDMF scheme against statistics derived from the LES. Section 6 compares results
 146 from the EDMF scheme against LES of canonical test cases of dry convective boundary
 147 layers, shallow and deep convection. Section 7 summarizes and discusses the main find-
 148 ings.

149 2 Extended EDMF Scheme

150 2.1 Equations of Motion

151 The extended EDMF scheme is derived from the compressible equations of motion
 152 of the host model. As thermodynamic variables, we choose the liquid-ice potential tem-
 153 perature θ_l and the total water specific humidity q_t , but these choices can easily be mod-
 154 ified and harmonized with the thermodynamic variables of the host model in which the
 155 scheme is implemented. The unfiltered governing equations are:

$$\frac{\partial \rho}{\partial t} + \nabla_h \cdot (\rho \mathbf{u}_h) + \frac{\partial(\rho w)}{\partial z} = 0, \quad (1)$$

$$\frac{\partial(\rho \mathbf{u}_h)}{\partial t} + \nabla_h \cdot (\rho \mathbf{u}_h \otimes \mathbf{u}_h) + \frac{\partial(\rho w \mathbf{u}_h)}{\partial z} = -\nabla_h p^\dagger + \rho S_{\mathbf{u}_h}, \quad (2)$$

$$\frac{\partial(\rho w)}{\partial t} + \nabla_h \cdot (\rho \mathbf{u}_h w) + \frac{\partial(\rho w w)}{\partial z} = \rho b - \frac{\partial p^\dagger}{\partial z} + \rho S_w, \quad (3)$$

$$\frac{\partial(\rho \theta_l)}{\partial t} + \nabla_h \cdot (\rho \mathbf{u}_h \theta_l) + \frac{\partial(\rho w \theta_l)}{\partial z} = \rho S_{\theta_l}, \quad (4)$$

$$\frac{\partial(\rho q_t)}{\partial t} + \nabla_h \cdot (\rho \mathbf{u}_h q_t) + \frac{\partial(\rho w q_t)}{\partial z} = \rho S_{q_t}, \quad (5)$$

$$p = \rho R_d T_v. \quad (6)$$

In the momentum equation, to improve numerical stability, we have removed a reference pressure profile $p_h(z)$ in hydrostatic balance with a density $\rho_h(z)$:

$$\frac{\partial p_h}{\partial z} = -\rho_h g,$$

where g is the gravitational acceleration. Therefore, the perturbation pressure

$$p^\dagger = p - p_h$$

and the buoyancy

$$b = -g \frac{\rho - \rho_h}{\rho}$$

156 appear in the momentum equations in place of the full pressure p and gravitational ac-
 157 celeration g . Otherwise, the notation is standard: ρ is density, q_t is the total water spe-
 158 cific humidity, T_v is the virtual temperature, R_d is the gas constant for dry air, and

$$\theta_l = T \left(\frac{p}{p_s} \right)^{R_d/c_p} \exp \left(\frac{L_v(q_l + q_i)}{c_p T} \right) \quad (7)$$

159 is the liquid-ice potential temperature, with liquid and ice specific humidities q_l and q_i
 160 and reference surface pressure $p_s = 10^5$ Pa. In a common approximation that can easi-
 161 ly be relaxed, we take the isobaric specific heat capacity of moist air c_p to be constant
 162 and, consistent with Kirchoff's law, the latent heat of vaporization L_v to be a linear
 163 function of temperature (Romps, 2008). The temperature T is obtained from the ther-
 164 modynamic variables θ_l , ρ , and q_t by a saturation adjustment procedure, and the vir-
 165 tual temperature T_v is computed from the temperature T and the specific humidities (Pressel
 166 et al., 2015). The horizontal velocity vector is \mathbf{u}_h , and w is the vertical velocity compo-
 167 nent; ∇_h is the horizontal nabla operator. The symbol S stands for sources and sinks.
 168 For the velocities, the sources $S_{\mathbf{u}_h}$ and S_w include the molecular viscous stress and Cori-
 169 olis forces, and for thermodynamic variables, the sources S_{θ_l} and S_{q_t} represent sources
 170 from molecular diffusivity, microphysics, and radiation.

171 2.2 Domain Decomposition and Subdomain Moments

172 The extended EDMF scheme is derived from the equations of motion by decom-
 173 posing the host model grid box into subdomains and averaging the equations over each
 174 subdomain volume. We denote by $\langle \phi \rangle$ the average of a scalar ϕ over the host model grid
 175 box, with $\phi^* = \phi - \langle \phi \rangle$ denoting fluctuations about the grid mean. Similarly, $\bar{\phi}_i$ is the
 176 average of ϕ over the i -th subdomain, and $\phi'_i = \phi - \bar{\phi}_i$ is the fluctuation about the mean
 177 of subdomain i . The difference between the subdomain mean and grid mean then be-
 178 comes $\bar{\phi}_i^* = \bar{\phi}_i - \langle \phi \rangle$. Common terminology assigns an area fraction $a_i = A_i/A_T$ to
 179 each subdomain, where A_i is the horizontal area of the i -th subdomain and A_T is the
 180 horizontal area of the grid box. This a_i is more precisely a volume fraction, since A_i is
 181 the vertically averaged horizontal area of the i -th subdomain within the grid box. We
 182 retain here the terminology using subdomain area fractions, which reflect the subdomain
 183 volume fractions, consistent with previous works (A. P. Siebesma et al., 2007).

184 With this decomposition, the subdomain zeroth moment (area fraction), first mo-
 185 ment (mean), centered second moment (covariance), and centered third moment obey:

$$\sum_{i \geq 0} a_i = 1, \quad (8)$$

$$\langle \phi \rangle = \sum_{i \geq 0} a_i \bar{\phi}_i, \quad (9)$$

$$\begin{aligned} \langle \phi^* \psi^* \rangle &= \sum_{i \geq 0} a_i \left[\bar{\phi}_i^* \bar{\psi}_i^* + \overline{\phi_i' \psi_i'} \right], \\ &= \sum_{i \geq 0} \left[a_i \overline{\phi_i' \psi_i'} + \frac{1}{2} \sum_{j \geq 0} a_i a_j (\bar{\phi}_i - \bar{\phi}_j) (\bar{\psi}_i - \bar{\psi}_j) \right], \end{aligned} \quad (10)$$

$$\begin{aligned} \langle \phi^* \psi^* w^* \rangle &= \sum_{i \geq 0} \left[a_i (\overline{\psi_i' \phi_i' w_i'} + \bar{\phi}_i \bar{\psi}_i \bar{w}_i + \bar{\psi}_i \overline{w_i' \phi_i'} + \bar{\phi}_i \overline{w_i' \psi_i'} + \bar{w}_i \overline{\psi_i' \phi_i'}) \right] \\ &\quad - \left[\langle \phi \rangle \langle \psi \rangle \langle w \rangle + \langle \phi \rangle \langle \psi^* w^* \rangle + \langle \psi \rangle \langle \phi^* w^* \rangle + \langle w \rangle \langle \psi^* \phi^* \rangle \right]. \end{aligned} \quad (11)$$

186 Equations (8) and (9) are self-evident; the derivation of (10) and (11) from (8) and (9)
 187 is given in Appendix A. Equation (10) with $\phi = w$ is the vertical SGS flux of a scalar
 188 ψ , which is one of the key predictands of any parameterization scheme: the divergence
 189 of this flux appears as a source in the equations for the resolved scales of the host model.
 190 The decomposition in (9)–(11) only applies in general if $(\bar{\cdot})$ is a Favre average—an av-
 191 erage weighted by the density that appears in the continuity equation. However, in the
 192 EDMF scheme we describe in what follows, we make the approximation of ignoring den-
 193 sity variations across subdomains (except in buoyancy terms), so that Favre and volume
 194 averages coincide within a grid box.

195 The central assumption in EDMF schemes is that within-subdomain covariances
 196 such as $\overline{\phi_i' \psi_i'}$ and higher moments are neglected in all subdomains except one distinguished
 197 subdomain, the environment, denoted by index $i = 0$. In the environment, covariances
 198 $\overline{\phi_0' \psi_0'}$ are retained, and third moments such as $\overline{w_0' \phi_0' \psi_0'}$, which appear in second-moment
 199 equations, are modeled with closures. The intuition underlying this assumption is that
 200 the flow domain is subdivided into an isotropically turbulent environment ($i = 0$) and
 201 into coherent structures, identified with plumes ($i \geq 1$). The environment can have sub-
 202 stantial within-environment covariances, whereas the plumes are taken to have compar-
 203 atively little variance within them. Variance within plumes can be represented by hav-
 204 ing an ensemble of plumes with different mean values (R. A. J. Neggers et al., 2002; R. Neg-
 205 gers, 2012; Sušelj et al., 2012). For the case of only two subdomains, an updraft ($i =$
 206 1) and its environment ($i = 0$), the second-moment equation (10) then simplifies to

$$\begin{aligned} \langle \phi^* \psi^* \rangle &= a_1 \overline{\phi_1' \psi_1'} + (1 - a_1) \overline{\phi_0' \psi_0'} + a_1 (1 - a_1) (\bar{\phi}_1 - \bar{\phi}_0) (\bar{\psi}_1 - \bar{\psi}_0) \\ &\approx \underbrace{(1 - a_1) \overline{\phi_0' \psi_0'}}_{\text{ED}} + \underbrace{a_1 (1 - a_1) (\bar{\phi}_1 - \bar{\phi}_0) (\bar{\psi}_1 - \bar{\psi}_0)}_{\text{MF}}, \end{aligned} \quad (12)$$

207 where the approximation in the second line reflects the EDMF assumption of neglect-
 208 ing within-plume covariances. The first equation states that the covariance on the grid
 209 scale can be decomposed into the sum of the covariances within subdomains and the co-
 210 variance among subdomain means, as in the analysis of variance (ANOVA) from statis-
 211 tics (Mardia et al., 1979). In the second line, the first term is closed by a down-gradient
 212 eddy diffusion (ED) closure; the second term is represented by a mass flux (MF) closure,
 213 whence EDMF derives its name (A. P. Siebesma & Teixeira, 2000). Similarly, under the
 214 EDMF assumption, the third-moment equation (11) for two subdomains, written for a
 215 single scalar, simplifies to

$$\langle \phi^* \phi^* \phi^* \rangle \approx -a_1 (1 - a_1) (\bar{\phi}_1 - \bar{\phi}_0) \overline{\phi_0' \phi_0'} + 3a_1 (1 - a_1) (1 - 2a_1) (\bar{\phi}_1 - \bar{\phi}_0)^3. \quad (13)$$

216 That is, third moments (i.e., skewness) on the grid scale are represented through covari-
 217 ances within the environment and through variations among means across subdomains
 218 with differing area fractions.

219

2.3 EDMF Assumptions

220

221

222

The extended EDMF scheme is obtained by applying this decomposition of grid-scale variations to the equations of motion (1)–(6), making the following additional assumptions:

223

224

225

226

1. We make the boundary layer approximation for subgrid scales, meaning that we assume vertical derivatives to be much larger than horizontal derivatives. This in particular means that the diffusive closure for fluxes in the environment only involves vertical gradients,

$$\overline{w'_i \phi'_i} \approx -K_{\phi,i} \frac{\partial \bar{\phi}_i}{\partial z}, \quad (14)$$

227

228

229

230

231

232

233

234

where $K_{\phi,i}$ is the eddy diffusivity (to be specified) for scalar ϕ in subdomain i . Consistent with the EDMF assumptions, we assume $K_{\phi,i} = 0$ for $i \neq 0$.

2. We use the same, grid-mean density $\langle \rho \rangle$ in all subdomains except in the buoyancy term. This amounts to making an anelastic approximation on the subgrid scale, to suppress additional acoustic modes that would otherwise arise through the domain decomposition. For notational simplicity, we use ρ rather than $\langle \rho \rangle$ for the grid-mean density in what follows, and $\bar{\rho}_i$ for the subdomain density that appears only in the buoyancy term:

$$\bar{b}_i = -g \frac{\bar{\rho}_i - \rho_h}{\rho}. \quad (15)$$

235

236

237

238

The grid-mean density ρ appears in the denominator, playing the role of the reference density in the anelastic approximation. The area fraction-weighted sum of the subdomain buoyancies is the grid-mean buoyancy, ensuring consistency of this decomposition:

$$\langle b \rangle = \sum_i a_i \bar{b}_i = -g \frac{\rho - \rho_h}{\rho}. \quad (16)$$

239

240

3. We take the subdomain horizontal velocities to be equal to their grid-mean values,

$$\bar{\mathbf{u}}_{h,i} = \langle \mathbf{u}_h \rangle. \quad (17)$$

241

242

243

This simplification is commonly made in parameterizations for climate models (Larson et al., 2019). It eliminates mass-flux contributions to the SGS vertical flux of horizontal momentum.

244

2.4 EDMF Equations

245

246

247

248

249

The full derivation of the subdomain-mean and covariance equations from (1)–(6) is given in Appendix B. The derivation largely follows Tan et al. (2018), except for a distinction between dynamical and turbulent entrainment and detrainment following de Rooy and Siebesma (2010). The resulting extended EDMF equation for the subdomain area fraction is

$$\frac{\partial(\rho a_i)}{\partial t} + \nabla_h \cdot (\rho a_i \langle \mathbf{u}_h \rangle) + \frac{\partial(\rho a_i \bar{w}_i)}{\partial z} = \sum_{j \neq i} (E_{ij} - \Delta_{ij}); \quad (18)$$

the equation for the subdomain-mean vertical momentum is

$$\begin{aligned} \frac{\partial(\rho a_i \bar{w}_i)}{\partial t} + \nabla_h \cdot (\rho a_i \langle \mathbf{u}_h \rangle \bar{w}_i) + \frac{\partial(\rho a_i \bar{w}_i \bar{w}_i)}{\partial z} = \\ \frac{\partial}{\partial z} \left(\rho a_i K_{w,i} \frac{\partial \bar{w}_i}{\partial z} \right) + \sum_{j \neq i} \left[(E_{ij} + \hat{E}_{ij}) \bar{w}_j - (\Delta_{ij} + \hat{\Delta}_{ij}) \bar{w}_i \right] \\ + \rho a_i (\bar{b}_i^* + \langle b \rangle) - \rho a_i \frac{\partial}{\partial z} \left(\frac{\bar{p}_i^* + \langle p^\dagger \rangle}{\rho} \right) + \bar{S}_{w,i}; \end{aligned} \quad (19)$$

and the equation for the subdomain-mean of scalar ϕ is

$$\begin{aligned} \frac{\partial(\rho a_i \bar{\phi}_i)}{\partial t} + \nabla_h \cdot (\rho a_i \langle \mathbf{u}_h \rangle \bar{\phi}_i) + \frac{\partial(\rho a_i \bar{w}_i \bar{\phi}_i)}{\partial z} = \\ \frac{\partial}{\partial z} \left(\rho a_i K_{\phi,i} \frac{\partial \bar{\phi}_i}{\partial z} \right) + \sum_{j \neq i} \left[(E_{ij} + \hat{E}_{ij}) \bar{\phi}_j - (\Delta_{ij} + \hat{\Delta}_{ij}) \bar{\phi}_i \right] + \rho a_i \bar{S}_{\phi,i}. \end{aligned} \quad (20)$$

250 The dynamical entrainment rate from subdomain j into subdomain i is E_{ij} , and the de-
 251 trainment rate from subdomain i into subdomain j is Δ_{ij} . In addition to dynamical en-
 252 trainment, there is turbulent entrainment from subdomain j into i , with rate \hat{E}_{ij} . Tur-
 253 bulent entrainment differentially entrains tracers but not mass (see Appendix B).

The pressure and buoyancy terms in the vertical momentum equation (19) are writ-
 ten as the sum of their grid-mean value and perturbations from their grid-mean value.
 These perturbations vanish when summed over all subdomains because $\sum_i a_i \bar{\phi}_i^* = 0$;
 hence, the grid-mean values of the pressure and buoyancy terms are recovered upon sum-
 ming over subdomains. Following Pauluis (2008), the pressure gradient term in (19) is
 written with $1/\rho$ inside the gradient to ensure energy conservation in our SGS anelas-
 tic approximation; see Appendix C for details. The subdomain density $\bar{\rho}_i$ that is essen-
 tial for the subdomain buoyancy is computed from the subdomain virtual temperature
 $\bar{T}_{v,i}$ using the ideal gas law with the grid-mean pressure $\langle p \rangle$:

$$\bar{\rho}_i = \frac{\langle p \rangle}{R_d \bar{T}_{v,i}}. \quad (21)$$

254 In analogy with the anelastic approximation Pauluis (2008), this formulation of the ideal
 255 gas law ensures that $\sum_i a_i \bar{\rho}_i \bar{T}_{v,i} = \rho \langle T_v \rangle$, while accounting for subdomain virtual tem-
 256 perature effects, which play a key role in the buoyancy of updrafts in shallow convection.

The scalar equation (20) is applied to any thermodynamic variable, with its cor-
 responding subdomain-averaged source $\bar{S}_{\phi,i}$ on the right-hand side. The terms on the
 left-hand side represent the explicit time tendencies and fluxes of the subdomain-means,
 which can be viewed as forming part of the dynamical core of the host model. The terms
 on the right-hand side are sources and sinks that require closure. The covariance equa-

tion for the environment becomes

$$\begin{aligned}
 \frac{\partial(\rho a_0 \overline{\phi'_0 \psi'_0})}{\partial t} + \nabla_h \cdot (\rho a_0 \langle \mathbf{u}_h \rangle \overline{\phi'_0 \psi'_0}) + \underbrace{\frac{\partial(\rho a_0 \bar{w}_0 \overline{\phi'_0 \psi'_0})}{\partial z}}_{\text{vertical transport}} = \\
 \underbrace{\frac{\partial}{\partial z} \left(\rho a_0 K_{\phi\psi,0} \frac{\partial \overline{\phi'_0 \psi'_0}}{\partial z} \right)}_{\text{turbulent transport}} + \underbrace{2 \rho a_0 K_{\phi\psi,0} \frac{\partial \bar{\phi}_0}{\partial z} \frac{\partial \bar{\psi}_0}{\partial z}}_{\text{turbulent production}} \\
 + \sum_{i>0} \left(\underbrace{-\hat{E}_{0i} \overline{\phi'_0 \psi'_0}}_{\text{turb. entrainment}} + \underbrace{\bar{\psi}_0^* \hat{E}_{0i} (\bar{\phi}_0 - \bar{\phi}_i) + \bar{\phi}_0^* \hat{E}_{0i} (\bar{\psi}_0 - \bar{\psi}_i)}_{\text{turb. entrainment production}} \right) \\
 + \sum_{i>0} \left(\underbrace{-\Delta_{0i} \overline{\phi'_0 \psi'_0}}_{\text{dyn. detrainment}} + \underbrace{E_{0i} (\bar{\phi}_0 - \bar{\phi}_i) (\bar{\psi}_0 - \bar{\psi}_i)}_{\text{dyn. entrainment flux}} \right) \\
 - \underbrace{\rho a_0 \overline{D_{\phi'\psi',0}}}_{\text{dissipation}} + \rho a_0 (\overline{\psi'_0 S'_{\phi,0}} + \overline{\phi'_0 S'_{\psi,0}}). \quad (22)
 \end{aligned}$$

257 Consistently with the EDMF assumption, we have assumed here that $\overline{\phi'_i \psi'_i} = 0$ for $i >$
 258 0 . Covariance equations of this form are used for the thermodynamic variances $\overline{\theta'^2_{i,0}}$ and
 259 $\overline{q'^2_{t,0}}$ and for their covariance $\overline{\theta'_{i,0} q'_{t,0}}$, which are needed in microphysics parameterizations.
 260 Note that some of the entrainment and detrainment terms are cross-subdomain coun-
 261 terparts of the vertical gradient terms. For example, the “dynamical entrainment,” “tur-
 262 bulent entrainment,” and “turbulent entrainment production” are the cross-subdomain
 263 counterparts of the “vertical transport,” “turbulent transport,” and “turbulent produc-
 264 tion,” respectively. The “dynamical entrainment flux” lacks any vertical counterpart. This
 265 term arises as a flux across a variable boundary in the conditional averaging process.

The subdomain turbulent kinetic energy (TKE) is defined as $\bar{e}_i = 0.5(\overline{u_i'^2} + \overline{v_i'^2} + \overline{w_i'^2})$, and the TKE equation for the environment is written as

$$\begin{aligned}
 \frac{\partial(\rho a_0 \bar{e}_0)}{\partial t} + \nabla_h \cdot (\rho a_0 \langle \mathbf{u}_h \rangle \bar{e}_0) + \frac{\partial(\rho a_0 \bar{w}_0 \bar{e}_0)}{\partial z} = \\
 \underbrace{\frac{\partial}{\partial z} \left(\rho a_0 K_{m,0} \frac{\partial \bar{e}_0}{\partial z} \right)}_{\text{turbulent transport}} + \underbrace{\rho a_0 K_{m,0} \left[\left(\frac{\partial \langle u \rangle}{\partial z} \right)^2 + \left(\frac{\partial \langle v \rangle}{\partial z} \right)^2 + \left(\frac{\partial \bar{w}_0}{\partial z} \right)^2 \right]}_{\text{shear production}} \\
 + \sum_{i>0} \left(\underbrace{-\hat{E}_{0i} \bar{e}_0}_{\text{turb. entrainment}} + \underbrace{\bar{w}_0^* \hat{E}_{0i} (\bar{w}_0 - \bar{w}_i)}_{\text{turb. entrainment production}} \right) \\
 + \sum_{i>0} \left(\underbrace{-\Delta_{0i} \bar{e}_0}_{\text{dyn. detrainment}} + \underbrace{\frac{1}{2} E_{0i} (\bar{w}_0 - \bar{w}_i) (\bar{w}_0 - \bar{w}_i)}_{\text{dyn. entrainment production}} \right) \\
 + \underbrace{\rho a_0 \overline{w'_0 b'_0}}_{\text{buoyancy production}} - \underbrace{\rho a_0 \left[u'_0 \frac{\partial}{\partial x} \left(\frac{p^\dagger}{\rho} \right)' + v'_0 \frac{\partial}{\partial y} \left(\frac{p^\dagger}{\rho} \right)' + w'_0 \frac{\partial}{\partial z} \left(\frac{p^\dagger}{\rho} \right)' \right]}_{\text{pressure term}} - \underbrace{\rho a_0 \overline{D_{e,0}}}_{\text{dissipation}}; \quad (23)
 \end{aligned}$$

266 see Appendix B in Lopez-Gomez et al. (2020) for a detailed derivation of the TKE equa-
 267 tion. We have used the EDMF assumption that $\bar{e}_i \approx 0$ for $i > 0$. The prognostic TKE
 268 is used for closures of the eddy diffusivity in the environment as described in Lopez-Gomez
 269 et al. (2020).

270

2.5 Effect on Grid Mean and Constraints on Entrainment/Detrainment

The conservation of mass and scalars in the host model grid box requires that by summing the EDMF equations over all subdomains, the equations for the grid-mean variables are recovered. The horizontal flux divergence terms that are included in the EDMF equations, $\nabla_h \cdot (\rho a_i \langle \mathbf{u}_h \rangle \bar{\phi}_i)$, represent the fluxes across the boundaries of the host model grid (see Appendix B) and, when summed over all subdomains, recover their grid-mean counterpart. Additionally, mass conservation requires that between two subdomains i and j , the entrainment and detrainment rates satisfy $(E_{ij} - \Delta_{ij}) + (E_{ji} - \Delta_{ji}) = 0$. For entrainment and detrainment of subdomain-mean properties, scalar conservation further requires that

$$E_{ij} = \Delta_{ji}, \quad (24)$$

271

so that when summing over two interacting subdomains, the entrainment and detrainment terms cancel out. Similarly, scalar conservation requires symmetry, $\hat{E}_{ij} = \hat{E}_{ji}$, for turbulent entrainment.

272

273

Taking these requirements into account, a summation of equation (20) over all subdomains yields the grid-mean scalar equation

$$\frac{\partial(\rho\langle\phi\rangle)}{\partial t} + \nabla_h \cdot (\rho\langle\mathbf{u}_h\rangle\langle\phi\rangle) + \frac{\partial(\rho\langle w\rangle\langle\phi\rangle)}{\partial z} = -\frac{\partial}{\partial z}(\rho\langle w^*\phi^*\rangle) + \rho\langle S_\phi\rangle. \quad (25)$$

This is the form of the equation solved by the dynamical core of the host model. Using the covariance decomposition (10), the divergence of the SGS flux in (25) is written as the sum of the eddy diffusivity and mass flux components:

$$\frac{\partial}{\partial z}(\rho\langle w^*\phi^*\rangle) = -\frac{\partial}{\partial z}\left(\rho a_0 K_{\phi,0} \frac{\partial \bar{\phi}_0}{\partial z}\right) + \frac{\partial}{\partial z} \sum_{i \geq 0} a_i (\bar{w}_i - \langle w \rangle) (\bar{\phi}_i - \langle \phi \rangle).$$

This illustrates the coupling between the dynamical core equations and the EDMF scheme. Similarly, the grid covariance equation follows by using the subdomain continuity equation (18), scalar-mean equation (20), and the scalar covariance equation (22) in the covariance decomposition (10), which yields:

$$\begin{aligned} \frac{\partial(\rho\langle\phi^*\psi^*\rangle)}{\partial t} + \nabla_h \cdot (\rho\langle\mathbf{u}_h\rangle\langle\phi^*\psi^*\rangle) + \frac{\partial(\rho\langle w\rangle\langle\phi^*\psi^*\rangle)}{\partial z} = \\ \frac{\partial}{\partial z}\left(\rho a_0 K_{\phi\psi,0} \frac{\partial \overline{\phi'_0\psi'_0}}{\partial z}\right) - \rho\langle w^*\psi^*\rangle \frac{\partial\langle\phi\rangle}{\partial z} - \rho\langle w^*\phi^*\rangle \frac{\partial\langle\psi\rangle}{\partial z} \\ - \rho\langle D_{\phi^*\psi^*}\rangle + \rho\langle\psi^*S_\phi^*\rangle + \rho\langle\phi^*S_\psi^*\rangle. \end{aligned} \quad (26)$$

274

Here, we substituted the triple correlation term by downgradient diffusion of environmental covariance. In general, this equation is not solved by the host model. However, the consistency of the summation over subdomains to produce it ensures that the second moments are conserved within the EDMF scheme.

275

276

277

278

The subdomain equations in the EDMF scheme require closures for dynamical entrainment and detrainment, turbulent entrainment, perturbation pressure, eddy diffusivity, for the various sources, and for covariance dissipation. The following section focuses on closures for dynamical and turbulent entrainment and detrainment. The perturbation pressure closure is given by the sum of a virtual mass effect, momentum convergence, and pressure drag, see equation (11) in Lopez-Gomez et al. (2020). The eddy diffusivity and mixing length closures are described in Lopez-Gomez et al. (2020).

279

280

281

282

283

284

285

3 Closures

Entrainment and detrainment closures are a topic of extensive research (de Rooy et al., 2013). Following de Rooy and Siebesma (2010), we distinguish dynamical and turbulent entrainment and detrainment components. Turbulent entrainment is typically represented by a diffusive horizontal flux, while diverse closures for dynamical entrainment

and detrainment are in use. It is common to write the dynamical entrainment and detrainment rates as a product of the vertical mass flux $\rho a_i \bar{w}_i$ and fractional entrainment/detrainment rates ϵ_{ij} and δ_{ij}

$$E_{ij} = \rho a_i \bar{w}_i \epsilon_{ij}, \quad (27)$$

and

$$\Delta_{ij} = \rho a_i \bar{w}_i \delta_{ij}. \quad (28)$$

286 Closures are then derived for the fractional rates ϵ_{ij} and δ_{ij} per unit length (they have
287 units of 1/length).

288 Various functional forms for the fractional rates ϵ_{ij} and δ_{ij} have been proposed in
289 the literature. For example:

- 290 • Based on experiments on dry thermals, Morton et al. (1956) suggested ϵ_{ij} to be
291 inversely proportional to the updraft radius. This relation has been used in sev-
292 eral closures (Kain & Fritsch, 1990; Bretherton et al., 2004).
- 293 • Using a perturbation-response experiment in LES of shallow convection, Tian and
294 Kuang (2016) found $\epsilon_{i0} \propto 1/(\bar{w}_i \tau)$ with a mixing timescale τ . Such an entrain-
295 ment rate was used by R. A. J. Neggers et al. (2002), Sušelj et al. (2012), and Langhans
296 et al. (2019) in shallow convection parameterizations.
- 297 • Gregory (2001) analyzed LES of shallow convection and suggested $\epsilon_{i0} \propto \bar{b}_i / \bar{w}_i^2$,
298 which was used by Tan et al. (2018) for shallow convection. The ratio \bar{w}_i / \bar{b}_i plays
299 the role of the timescale τ in the formulation of Tian and Kuang (2016). In the
300 steady equations, this entrainment functional also ensures that the mass flux and
301 the vertical velocity simultaneously go to zero at the top of updrafts; see Appendix
302 E and Romps (2016). Alternative derivations of this functional form are based on
303 a balance of sources and sinks of total kinetic energy in updrafts Savre and Her-
304 zog (2019), or on the dynamics of dry thermals (McKim et al., 2020).
- 305 • Other approaches for entrainment and detrainment include stochastic closures (Sušelj
306 et al., 2013; Suselj et al., 2014; Romps, 2016; Suselj et al., 2019a) and higher-order
307 closures (Lappen & Randall, 2001b).

308 Similar closures are often used for both entrainment ϵ_{ij} and detrainment rates δ_{ij} .
309 Enhanced detrainment can occur in cloudy conditions: when the evaporation of cloud
310 condensate after mixing with drier environmental air produces a buoyancy sink for an
311 updraft, negatively buoyant air can detrain rapidly from the updraft (Raymond & Blyth,
312 1986; Kain & Fritsch, 1990). Various approaches for representing this enhanced detrain-
313 ment owing to “buoyancy sorting” have been used, ranging from adding a constant back-
314 ground detrainment rate A. Siebesma and Cuijpers (1995); Tan et al. (2018), over ex-
315 plicitly modeling buoyancies of mixtures of cloudy and environmental air (Kain & Fritsch,
316 1990; Bretherton et al., 2004), to enhancing detrainment by functions of updraft-environment
317 relative humidity differences (Böing et al., 2012; Bechtold et al., 2008, 2014; Savre & Her-
318 zog, 2019).

319 Here we combine insights from several of these studies into a new closure for en-
320 trainment and detrainment.

321 3.1 Dynamical Entrainment and Detrainment

322 We propose closures for dynamical entrainment and detrainment that are in prin-
323 ciple applicable to many interacting subdomains (e.g., multiple updrafts, or updrafts and
324 downdrafts). Our point of departure are dry entrainment and detrainment rates, which
325 are symmetric for upward and downward motions. To those we then add the contribu-
326 tion of evaporation, which is asymmetric between upward and downward motions. We
327 first write our closures for the rates E_{ij} and Δ_{ij} , which facilitates ensuring mass and scalar

Table 1. Closure parameters

Symbol	Description	Value (units)
a_s	Combined updraft surface area fraction	0.1
c_ϵ	Scaling constant for entrainment rate	0.13
c_δ	Scaling constant for detrainment rate	0.52
c_λ	Weight of TKE term in entrainment/detrainment rate	0.3
β	Detrainment relative humidity power law	2.0
μ_0	Timescale for b/w in the entrainment sigmoidal function	4×10^{-4} (1/s)
χ_i	Fraction of updraft air in buoyancy mixing	0.25
c_γ	Scaling constant for turbulent entrainment rate	0.075

328 conservation. In the end, we give the corresponding formulations in terms of the frac-
 329 tional rates ϵ_{ij} and δ_{ij} .

330 3.1.1 General Form of Entrainment and Detrainment Rates

The rates E_{ij} and Δ_{ij} have units of density divided by time and hence depend on a flow-dependent time scale, as well as on functions of nondimensional groups in the problem. Following Gregory (2001); Tan et al. (2018); Savre and Herzog (2019); McKim et al. (2020), among others, we choose an inverse timescale b/w as the fundamental scale, depending on a buoyancy b and a vertical velocity w . We combine it with a counterpart scale in which the vertical velocity w is replaced by the environmental turbulent velocity scale $\bar{e}_0^{1/2}$. Considerations of symmetry and mass and tracer conservation lead to an inverse timescale

$$\lambda_{ij} = s_{\min} \left(\left| \frac{\bar{b}_i - \bar{b}_j}{\bar{w}_i - \bar{w}_j} \right|, c_\lambda \left| \frac{\bar{b}_i - \bar{b}_j}{\sqrt{\bar{e}_0}} \right| \right). \quad (29)$$

Here, $\lambda_{ij} = \lambda_{ji}$, c_λ is a nondimensional fitting parameter, and s_{\min} is the smooth minimum function defined in Lopez-Gomez et al. (2020). The smooth minimum function ensures that the strongest characteristic velocity defines the entrainment rate. The inverse time scale λ_{ij} depends on the buoyancy difference $\bar{b}_i - \bar{b}_j$ between subdomains i and j , as is physical. Similarly, it depends only on the mean vertical velocity difference $\bar{w}_i - \bar{w}_j$, as is required by Galilean invariance. In terms of this inverse time scale, the entrainment and detrainment rates are then written as

$$E_{ij} = \rho \lambda_{ij} \left(c_\epsilon \mathcal{D}_{ij} + c_\delta \mathcal{M}_{ij} \right), \quad (30)$$

and

$$\Delta_{ij} = \rho \lambda_{ij} \left(c_\epsilon \mathcal{D}_{ji} + c_\delta \mathcal{M}_{ji} \right). \quad (31)$$

331 Mass and tracer conservation demand that $E_{ij} = \Delta_{ji}$ (see Eq. (24)). This is satisfied
 332 by this formulation: The inverse time scale λ_{ij} is symmetric under reversal of the i and
 333 j indices by construction. Conservation constraints are satisfied by the choice of the, as
 334 yet unspecified, nondimensional functions \mathcal{D}_{ij} and \mathcal{M}_{ji} in the entrainment rate (30) and,
 335 with inverted indices, \mathcal{D}_{ji} and \mathcal{M}_{ij} in the detrainment rate (31). The coefficients c_ϵ and
 336 c_δ are nondimensional fitting parameters. The functions \mathcal{D}_{ij} and \mathcal{M}_{ij} in principle can
 337 depend on all nondimensional groups of the problem. Once sufficient data are available,
 338 be they from high-resolution simulations or observations, they can be learned from data.

339 To demonstrate the viability of the EDMF closure, we use physically motivated and
 340 relatively simple functions for \mathcal{D}_{ij} and \mathcal{M}_{ij} .

341

3.1.2 Function \mathcal{D}_{ij}

We use the function \mathcal{D}_{ij} to partition the relative magnitudes of entrainment and detrainment for a subdomain i in dry convection, based on buoyancy sorting ideas (Kain & Fritsch, 1990; Bretherton et al., 2004). We consider the buoyancy \bar{b}_{mix} of a mixture, composed of a fraction χ_i of air from subdomain i , and a fraction χ_j of air from subdomain j (with $\chi_i + \chi_j = 1$). We define an inverse timescale based on the mixture buoyancy as

$$\mu_{ij} = \frac{\bar{b}_{\text{mix}} - \bar{b}_{ij}}{\bar{w}_i - \bar{w}_j}, \quad (32)$$

where

$$\bar{b}_{ij} = \frac{a_i \bar{b}_i + a_j \bar{b}_j}{a_i + a_j} \quad (33)$$

is the area-weighted mean buoyancy of subdomains i and j , such that $a_i + a_j = 1$ implies $\bar{b}_{ij} = \langle b \rangle$. (Note that we are assuming dry conditions here, so buoyancy averages linearly.) Here $\mu_{ij} = -\mu_{ji}$, and its sign reflects the correlation between the sign of the velocity difference $\bar{w}_i - \bar{w}_j$ and the sign of the mixture buoyancy \bar{b}_{mix} relative to the mean buoyancy \bar{b}_{ij} . The mixture buoyancy is defined as

$$\bar{b}_{\text{mix}} = \chi_i \bar{b}_i + \chi_j \bar{b}_j, \quad (34)$$

so that the buoyancy difference in (32) becomes

$$\bar{b}_{\text{mix}} - \bar{b}_{ij} = (\bar{b}_i - \bar{b}_j) \left(\chi_i - \frac{a_i}{a_i + a_j} \right), \quad (35)$$

342

which follows by using $\chi_i = 1 - \chi_j$.

Thus we assumed that the more rapidly rising subdomain entrains air if the mixture buoyancy is positive relative to the mean of the two interacting subdomains, and vice versa. This means that we expect entrainment from subdomain j into i if $\mu_{ij} > 0$, and we expect detrainment otherwise. This could be modeled by choosing $\mathcal{D}_{ij} = \max(\mu_{ij}, 0)$. However, we find that using a smooth sigmoidal function, between 0 and 1, improves our results, so we define

$$\mathcal{D}_{ij} = \frac{1}{1 + e^{-\mu_{ij}/\mu_0}}. \quad (36)$$

343

Here, μ_0 is an inverse timescale, a fitting parameter that controls the smoothness of the sigmoidal function. We estimate $\mu_0 = 4 \times 10^{-4} \text{ s}^{-1}$ from examining various LES test cases. The fraction of air in the mixture, χ_i , is typically taken from an assumed probability distribution (Kain, 2004; Bretherton et al., 2004). Here we choose a constant χ_i value based on a heuristic assumption of an elliptical updraft in a surrounding mixing shell. If the mixing eddies at the updraft edge have similar radial extent in the updraft and in the shell, it implies that χ_i is proportional to the ratio between the updraft area and the combined updraft and shell area; that is, $\chi_i = 0.25$.

349

350

351

3.1.3 Function \mathcal{M}_{ij}

In moist conditions, the function \mathcal{M}_{ji} represents the enhancement of detrainment from the rising subdomain i (and entrainment into the sinking subdomain j) by evaporation of liquid water when i is cloudy (saturated). In dry conditions, we expect $\mathcal{M}_{ji} = \mathcal{M}_{ij} = 0$. Similar to Savre and Herzog (2019), the evaporative potential of the drier subdomain j , is approximated here by an ad hoc function of the difference between the relative humidities RH_i and RH_j of the subdomains, conditioned on the saturation of subdomain i :

$$\mathcal{M}_{ji} = \begin{cases} \left[\max(\overline{\text{RH}}_i^\beta - \overline{\text{RH}}_j^\beta, 0) \right]^{\frac{1}{\beta}}, & \text{if } \overline{\text{RH}}_i = 1, \\ 0, & \text{if } \overline{\text{RH}}_i < 1. \end{cases} \quad (37)$$

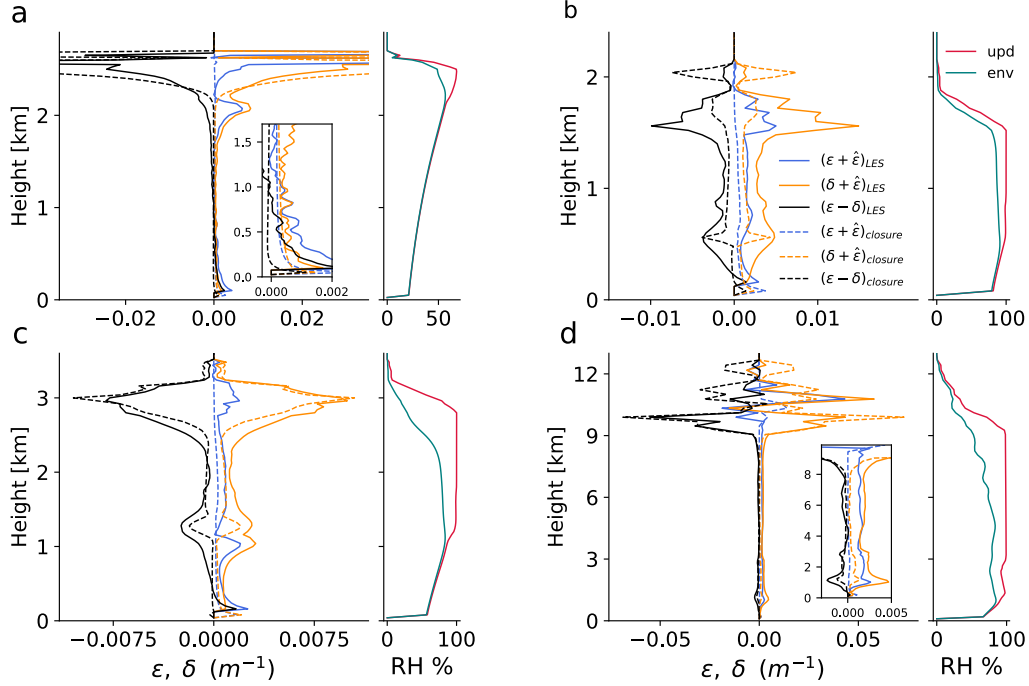


Figure 1. A comparison of the direct estimates (“LES,” solid lines) of fractional entrainment and detrainment rates and their closures (“closure,” dashed lines) evaluated in LES of the four convective test cases. Panels (a), (b), (c), and (d) show results for the DCBL, BOMEX, ARM-SGP and TRMM LBA test cases. For each case, the left panel shows the mean profiles of diagnosed entrainment, detrainment, and their net rate (solid lines), averaged over the last two hours (hours 9–11 in ARM-SGP), compared with the closures in (38), (39), and (40) (dashed lines). The right panel for each case shows profiles of relative humidity in the updraft (red) and environment (green). The legend in (b) applies to all panels.

352 Here, β is a nondimensional parameter that controls the magnitude of the evaporative
 353 potential for a given relative humidity difference. With this closure, a saturated updraft
 354 i detrains when the environment $j = 0$ is subsaturated, and the detrainment rate in-
 355 creases with increasing subsaturation of the environment.

356 3.1.4 Fractional Entrainment and Detrainment Rates

Given the relationships (27) and (28) between the entrainment rates E_{ij} and D_{ij} and their fractional counterparts ϵ_{ij} and δ_{ij} , the fractional rates are

$$\epsilon_{ij} = \frac{E_{ij}}{\rho a_i \bar{w}_i} = \frac{\lambda_{ij}}{a_i \bar{w}_i} \left(c_\epsilon \mathcal{D}_{ij} + c_\delta \mathcal{M}_{ij} \right), \quad (38)$$

and

$$\delta_{ij} = \frac{D_{ij}}{\rho a_i \bar{w}_i} = \frac{\lambda_{ij}}{a_i \bar{w}_i} \left(c_\epsilon \mathcal{D}_{ji} + c_\delta \mathcal{M}_{ji} \right). \quad (39)$$

The relationship $E_{ij} = D_{ji}$ required for scalar and mass conservation in terms of the fractional rates implies

$$\delta_{ji} = \frac{a_i \bar{w}_i}{a_j \bar{w}_j} \epsilon_{ij}.$$

The difference between the fractional rates, which gives the rate of change of mass fluxes in updrafts with height, is

$$\epsilon_{ij} - \delta_{ij} = \frac{\lambda_{ij}}{a_i \bar{w}_i} \left(c_\epsilon (\mathcal{D}_{ij} - \mathcal{D}_{ji}) + c_\delta (\mathcal{M}_{ji} - \mathcal{M}_{ij}) \right). \quad (40)$$

357

The function $\mathcal{D}_{ij} - \mathcal{D}_{ji}$ appearing here is a sigmoidal function between -1 and 1 .

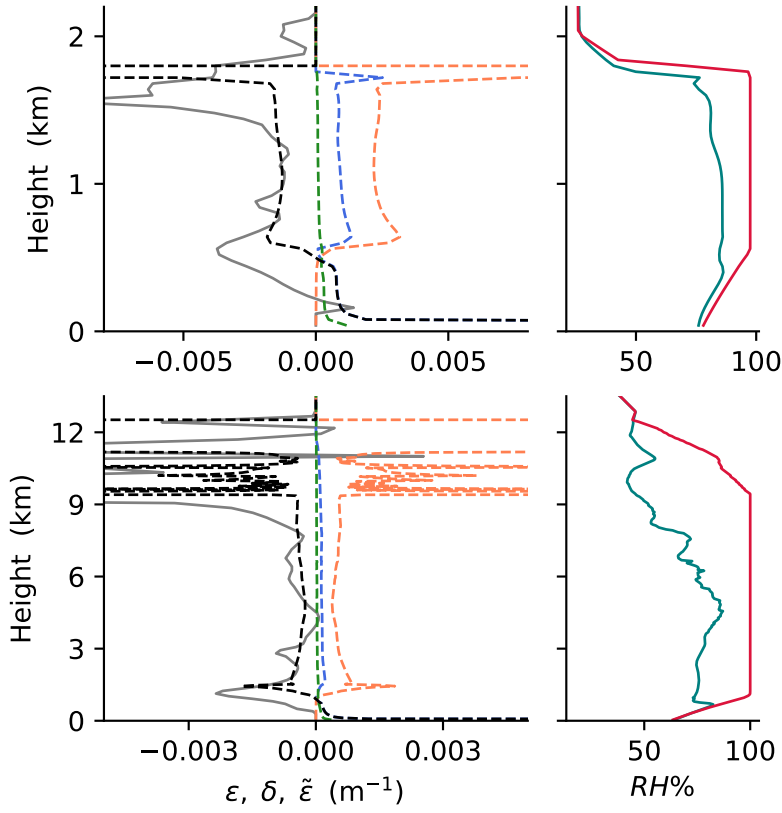


Figure 2. Last two hours mean profiles of entrainment and detrainment in the SCM simulations of BOMEX (top) and TRMM-LBA (bottom): dynamic entrainment rate ϵ (dashed-blue), dynamic detrainment rate δ (dashed-orange), net entrainment rate $\epsilon - \delta$ (dashed-black), and turbulent entrainment $\tilde{\epsilon}$ (dashed-green). The LES-diagnosed $\epsilon - \delta$, as in Figure 1, is added in solid-gray for comparison. The corresponding relative humidities (RH) of the updraft (red) and environment (green) are shown on the right-hand side.

358

For the situation where entrainment is only considered between an updraft i and the environment $j = 0$, and if the environmental mean vertical velocity \bar{w}_0 and turbulent kinetic energy \bar{e}_0 are neglected, this closure reduces to a closure of the form \bar{b}_i / \bar{w}_i^2 .

359

360

361 It is heuristically modulated by the nondimensional functions \mathcal{D}_{ij} and \mathcal{M}_{ij} , which par-
 362 tition between entrainment and detrainment in the dry case and account for enhanced
 363 detrainment owing to evaporation of condensate.

364 3.2 Turbulent Entrainment

We assume that turbulent entrainment takes place only between the plumes (up-
 drafts and downdrafts) and their environment, where second moments are not neglected.
 Therefore, we assume it depends on the turbulent velocity scale of the environment, $\sqrt{\bar{e}_0}$,
 and the radial scale of a plume R_i . The turbulent entrainment rate is related to the flux
 across the subdomain boundary via

$$\hat{E}_{i0}(\bar{\phi}_0 - \bar{\phi}_i) = -\rho a_i \frac{A_{sg}}{V_i} \widehat{\phi' u'_{r,n}}, \quad (41)$$

where A_{sg} and V_i are the updraft's interface area and volume (see the derivation of (B10)).
 We assume here that the updraft is cylindrical with a circular cross section, so that the
 ratio between its interface area and its volume is $A_{sg}/V_i = 2/R_i$. Following de Rooy
 and Siebesma (2010); Asai and Kasahara (1967) and Kuo (1962) the outwards pointing
 turbulent flux across the boundary of the i -th updraft, $\widehat{\phi' u'_{r,n}}$, is modelled by downgra-
 dient eddy diffusion

$$\widehat{\phi' u'_{r,n}} \approx -\hat{K}_{i0} \frac{\bar{\phi}_0 - \bar{\phi}_i}{R_i} = -\hat{K}_{i0} \frac{\bar{\phi}_0 - \bar{\phi}_i}{\gamma H_i}. \quad (42)$$

Here \hat{K}_{i0} is the entrainment eddy diffusivity between the environment and the i -th sub-
 domain. The cross-subdomain gradient is discretized using the difference in the mean
 values of the two interacting subdomains and the radial scale of the updraft R_i . The lat-
 ter is written in terms of updraft height H_i and an aspect ratio γ as $R_i = \gamma H_i$. For the
 entrainment eddy diffusivity, we assume the form

$$\hat{K}_{i0} = c_t R_i \sqrt{\bar{e}_0}, \quad (43)$$

365 where R_i is used as a mixing length and c_t is a non-dimensional fitting parameter.

Combining equations (41)–(43), we obtain the turbulent entrainment rate

$$\hat{E}_{i0} = 2\rho a_i \left(\frac{c_t}{\gamma} \right) \frac{\sqrt{\bar{e}_0}}{R_i} = 2\rho a_i c_\gamma \frac{\sqrt{\bar{e}_0}}{H_i}, \quad (44)$$

where $c_\gamma = c_t/\gamma$ is a fitting parameter that combines c_t and γ (Table 1). The middle
 term in (44) shows that $\hat{E}_{ij} \propto 1/R_i$, in agreement with laboratory experiments of dry
 plumes (Morton et al., 1956; Turner, 1963). It is also useful to define a fractional coun-
 terpart for turbulent entrainment,

$$\hat{\epsilon}_{i0} = \frac{\hat{E}_{ij}}{\rho a_i \bar{w}_i} = \frac{2c_\gamma \sqrt{\bar{e}_0}}{\bar{w}_i H_i}. \quad (45)$$

366 4 Numerical Implementation

367 The model equations and closures are implemented in the single column model (SCM)
 368 used in Tan et al. (2018), where a detailed description of the implementation of the ini-
 369 tial and boundary conditions is given. The model solves for first moments of the prog-
 370 nostic variables $\{a_i, \bar{w}_i, \bar{\theta}_{l,i}, \bar{q}_{t,i}\}$ in updrafts using (18), (19), and (20), respectively, and
 371 for the grid mean variables $\{\langle \theta_l \rangle, \langle q_t \rangle\}$ using equations of the form of (25), in which pre-
 372 scribed large-scale tendencies are applied as sources.

373 We consider a single updraft and its turbulent environment. The mean environ-
 374 mental properties are computed diagnostically as the residual of updraft and grid-mean

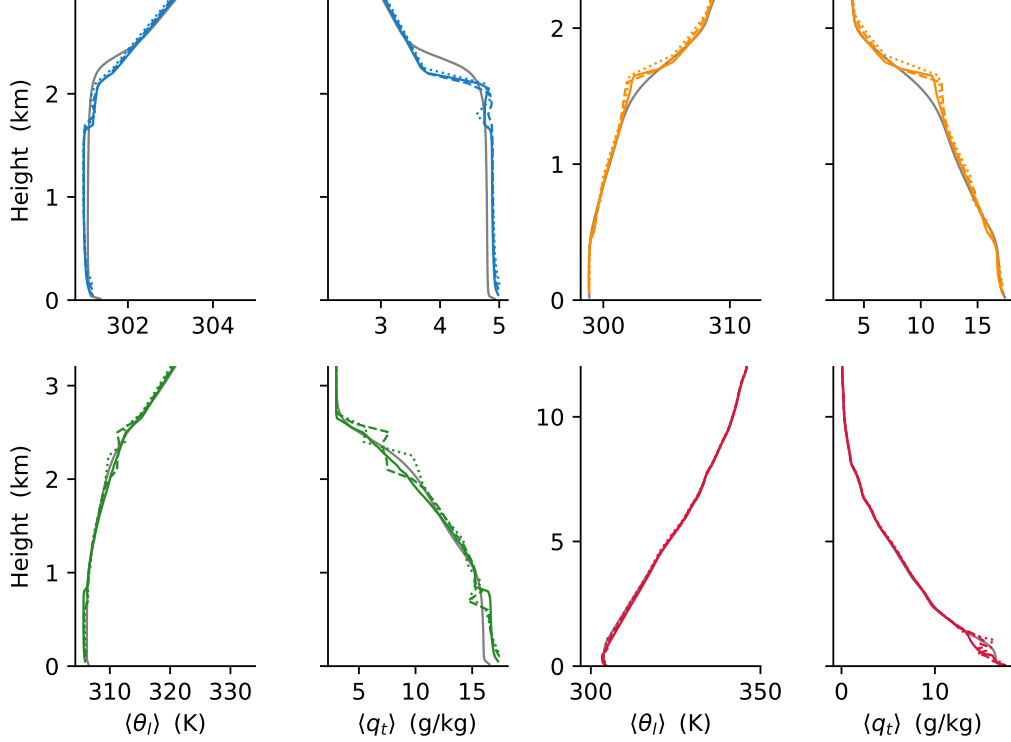


Figure 3. Comparison of SCM and LES for the last two hours (hours 9–11 in ARM-SGP) for mean profiles of first moments $\langle \theta_t \rangle$ and $\langle q_t \rangle$. In all panels, color lines show SCM profiles and grey lines represent the corresponding LES profiles. DCBL, BOMEX, ARM-SGP, and TRMM-LBA are color-coded as blue, orange, green, and red. Solid, dashed and dotted color lines show SCM results for 50 m, 100 m and 150 m resolutions, respectively.

375 quantities using (8) and (9). Prognostic equations for the second moments in the envi-
 376 ronment are solved using (22) and (23). The grid-scale second moments are diagnosed
 377 from (10), using the EDMF assumption of neglecting second moments in the updraft.
 378 Grid-scale third moments are diagnosed using (11), neglecting third moments in all in-
 379 dividual subdomains. Thus, from a probability density function perspective, we are us-
 380 ing a closure model that assumes a Gaussian environment and a delta distribution up-
 381 draft (Lappen & Randall, 2001a).

382 The initial conditions, surface fluxes, and large-scale forcing are case specific. They
 383 are taken from the papers describing the cases, are linearly interpolated to the model
 384 resolution, and are implemented identically in the SCM and LES.

The implementation of the SCM is fully anelastic, in contrast to the SGS anelas-
 tic approximation described in Appendix C; that is, the SCM does not solve for the grid-
 mean density and pressure. This amounts to substituting ρ by ρ_h in the EDMF subdo-
 main equations, and consequently in the buoyancy definition (15). In addition, since $\langle w \rangle =$
 0 in the SCM, the grid-mean is hydrostatic

$$\langle b \rangle = \frac{\partial}{\partial z} \left(\frac{\langle p^\dagger \rangle}{\rho_h} \right), \quad (46)$$

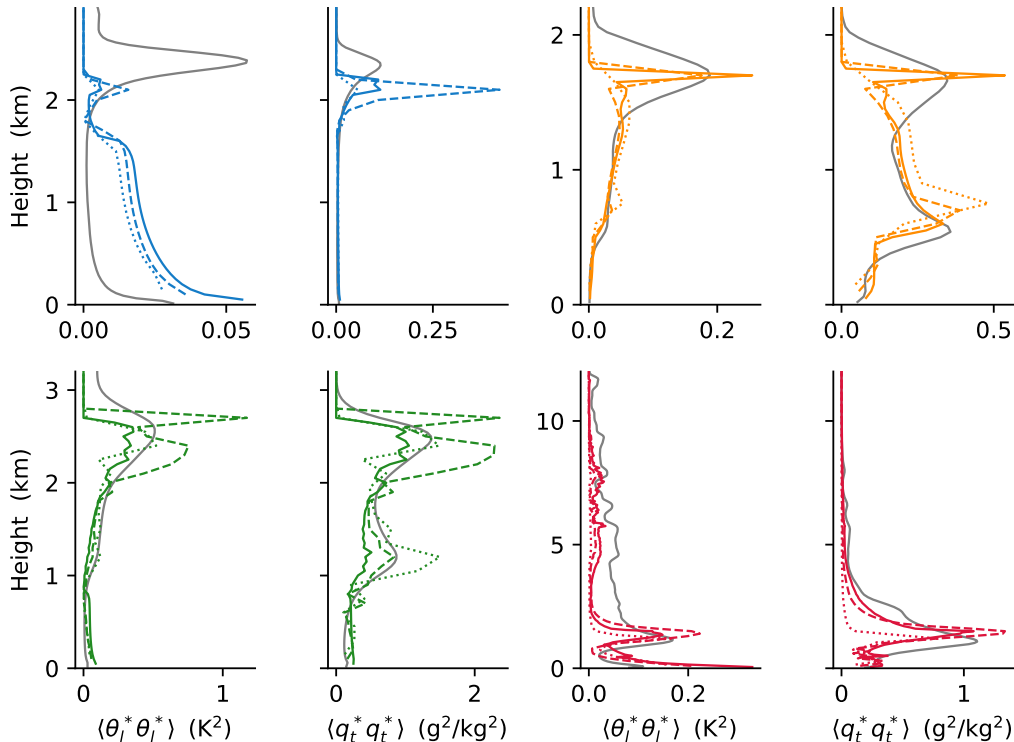


Figure 4. Same as Figure 3 but for the second moments: $\langle \theta_i^* \theta_i^* \rangle$ and $\langle q_t^* q_t^* \rangle$.

385 thus removing from the subdomain equations the dependence on the grid-mean pressure.
 386 Furthermore, the grid-mean anelastic approximation requires the use of the reference pres-
 387 sure ($\langle p \rangle = p_h$) in the ideal gas law (21) for consistency (Pauluis, 2008).

388 The set of parameters used in all simulations in this paper is listed in Table 1. All
 389 SCM simulations use a uniform vertical resolution of 50 m, with results from a resolu-
 390 tion sensitivity test at 100 m and 150 m shown for the first three moments in the grid.
 391 Other implementation details, such as how cloud properties are computed via numer-
 392 ical quadrature over implied SGS distributions, are described in Lopez-Gomez et al. (2020).

393 5 Large-Eddy Simulations and Diagnosis of EDMF Subdomains

394 To assess the performance of the extended EDMF scheme, we compared it with LES
 395 in four convective test cases. We use PyCLES Pressel et al. (2015), an anelastic LES code
 396 with weighted essentially non-oscillatory (WENO) numerics. We use an implicit LES strat-
 397 egy, which uses the dissipation inherent to WENO schemes as the only subgrid-scale dis-
 398 sipation. Such an implicit LES has been shown to outperform explicit SGS closures in
 399 simulations of low clouds (Pressel et al., 2017; Schneider et al., 2019). We use passive
 400 tracers that decay in time to diagnose updrafts and their exchanges with the environ-
 401 ment in the LES (see Appendix D).

402 Four standard convective test cases are considered here: dry convective boundary
 403 layer, maritime shallow convection, continental shallow convection, and continental deep
 404 convection.

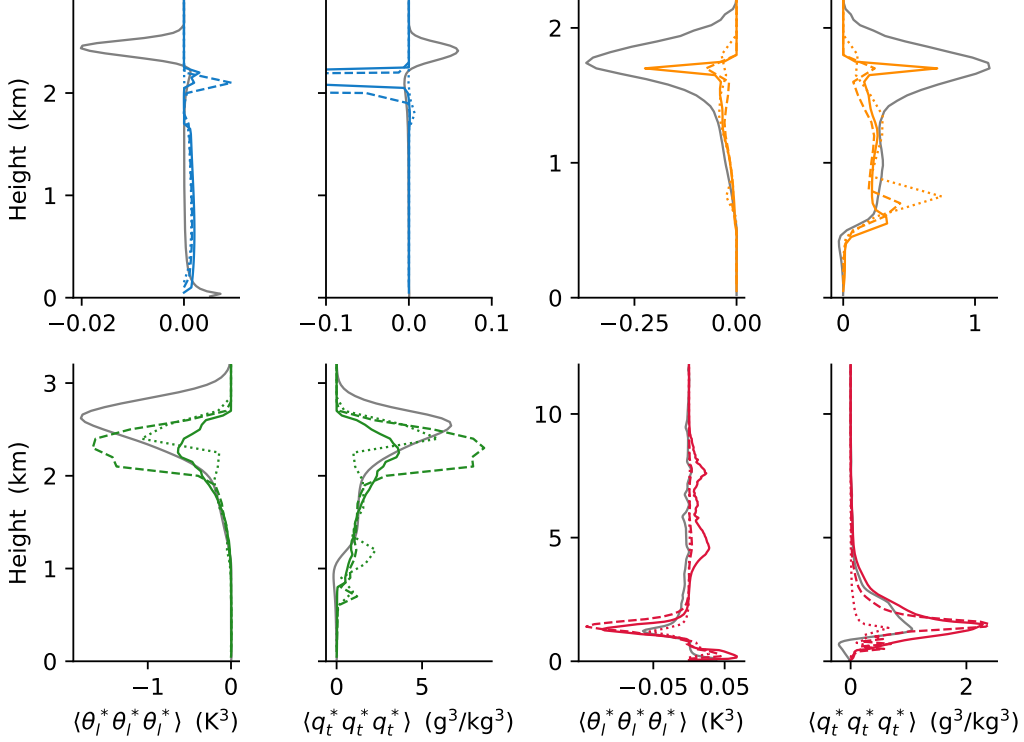


Figure 5. Same as Figure 3 but for the third moments $\langle \theta_i^* \theta_j^* \theta_l^* \rangle$ and $\langle q_i^* q_t^* q_t^* \rangle$. The DCBL spike in the $\langle q_i^* q_t^* q_t^* \rangle$ profile (blue) has an amplitude of $-1.5 (g^3/gk^3)$.

- 405 1. The Dry Convective Boundary Layer (DCBL, blue lines in all figures) case is based
406 on Soares et al. (2004). In this case, convection develops through 8 hours from an
407 initially neutral profile below 1350 m (which is stable above it) with prescribed
408 sensible and latent heat fluxes and negligible large scale winds. We use an isotropic
409 25 m resolution in a $6.4 \times 6.4 \text{ km} \times 3.75 \text{ km}$ domain.
- 410 2. The marine shallow convection test case is based on the Barbados Oceanographic
411 and Meteorological Experiment (BOMEX, orange lines) described in Holland and
412 Rasmusson (1973). In this case, large-scale subsidence drying and warming and
413 fixed surface fluxes are prescribed, and shallow cumulus convection evolves over
414 6 hours, with a quasi-steady state maintained in the last 3 hours (A. P. Siebesma
415 et al., 2003). We use an isotropic 40 m resolution in a $6.4 \text{ km} \times 6.4 \text{ km} \times 3 \text{ km}$
416 km domain.
- 417 3. The continental shallow convection test case is based on the Atmospheric Radiation
418 Measurement Program at the Southern Great Plains site (ARM-SGP, green
419 lines) described in Brown et al. (2002). This case exhibits a diurnal cycle of the
420 surface fluxes, with cumulus convection first developing and then decaying between
421 5:30 and 20:00 local time. We use $100 \text{ m} \times 100 \text{ m} \times 40 \text{ m}$ resolution in a $25 \text{ km} \times$
422 $25 \text{ km} \times 4 \text{ km}$ domain. The large surface fluxes of latent and sensible heat erode
423 the initial inversion as convection penetrates into the free atmosphere (Brown et
424 al., 2002).
- 425 4. The continental deep convection test case is based on the Large-scale Biosphere-
426 Atmosphere experiment with data from the Tropical Rainfall Measurement Mis-
427 sion (TRMM-LBA, red lines) observed on 23 February 1999 (Grabowski et al., 2006).
428 In this case, prescribed time-varying surface fluxes and radiative cooling profiles

429 force a diurnal cycle, during which shallow convection transitions into deep con-
 430 vection in the 6 hours between 7:30 and 13:30 local time. We use $200\text{ m} \times 200\text{ m} \times$
 431 50 m resolution in a $51.2\text{ km} \times 51.2\text{ km} \times 24\text{ km}$ domain. No subsidence drying
 432 or warming are prescribed in this case. In our simulations of the TRMM-LBA case,
 433 microphysical rain processes are modelled by a simple warm-rain cutoff scheme
 434 that removes liquid water once it is 2% supersaturated. This simple scheme is im-
 435 plemented in the LES for a direct comparison with the same simple microphysics
 436 scheme in SCM. In future work, we will implement a more realistic microphysics
 437 scheme.

438 The different cases span a wide range of conditions that allow us to examine the
 439 different components of the unified entrainment and detrainment formulation presented
 440 in section 3. The DCBL case allows us to examine the dry formulations for dynamic and
 441 turbulent entrainment irrespective of the moisture related detrainment. The differences
 442 in environmental humidity between the shallow and deep convection cases allows us to
 443 test the moisture-dependent detrainment closure. For instance, we found the bulk de-
 444 trainment value used in previous parameterization evaluated with BOMEX A. Siebesma
 445 and Cuijpers (1995); Tan et al. (2018) to be excessive for TRMM-LBA.

446 The diagnosis of the direct estimates of entrainment and detrainment and compar-
 447 ison with the closures (38) and (39) relies on decaying tracers with a surface source, which
 448 uniquely identify each LES grid box as either updraft or environment. Here we use the
 449 tracer scheme described in Couvreux et al. (2010), which labels a grid cell as updraft if
 450 its vertical velocity, tracer concentration, and liquid water specific humidity (above cloud
 451 base) exceed given thresholds. The net of entrainment minus detrainment [right-hand
 452 side of (18)] is diagnosed using the area and vertical velocity of updrafts identified with
 453 the help of the tracer scheme. Fractional entrainment is diagnosed based on an advective
 454 form of the scalar equation, see Eq. (D1). Further information on the diagnosis is
 455 found in Appendix D.

456 6 Results

457 A comparison of the closures for the fractional turbulent and dynamic entrainment
 458 and detrainment rates with direct estimates of these terms from LES is shown in Fig-
 459 ure 1. The profiles of the closures for entrainment and detrainment are similar to the
 460 direct estimates from LES. The role of the environmental moisture deficit in enhancing
 461 detrainment in the cloud layer is consistent with the directly diagnosed detrainment in
 462 ARM-SGP, in which convection penetrates into a dry layer with $\text{RH} \approx 50\%$.

463 When implemented in the SCM, these closures perform in a similar manner (Fig-
 464 ure 2). Entrainment prevails in the sub-cloud layer while detrainment prevails in the cloud
 465 layer, owing to the large environmental moisture deficit. The value of $\epsilon - \delta$ predicted
 466 by the closures in the EDMF scheme is in agreement with direct estimates of this value
 467 from LES (solid gray lines).

468 We now turn to compare the performance of the EDMF scheme with LES. First,
 469 second, and third moments of θ_t and q_t are compared in Figures 3, 4, and 5. These show
 470 overall good matches between the SCM and LES, with a few notable mismatches. For
 471 example, in first moments in the sub-cloud layer in the ARM-SGP case, at cloud top in
 472 the BOMEX case, and at the top of the DCBL; in second moments ($\langle \theta_t^{*2} \rangle$) throughout
 473 the DCBL; and in the third moments at the overshoots. Moreover, mismatches in sign
 474 are seen for $\langle \theta_t^{*3} \rangle$ in SCM simulations of TRMM-LBA at mid levels, and for $\langle q_t^{*3} \rangle$ at the
 475 top of the DCBL. The sensitivity test in 100 m (dashed color lines) and 150 m (dotted
 476 color lines) in these figures shown that these results are generally robust to the vertical
 477 resolutions expected in the host model.

478 The grid-mean fluxes, whose divergence is a source in the host model equations,
 479 are shown in Figure 6. We find good agreement in the fluxes except for $\langle w^* \theta_l^* \rangle$ in TRMM-
 480 LBA at mid levels, where the SCM shows a strongly negative flux while the LES has a
 481 negligible flux there. The ED and MF components of the SCM fluxes show that in moist
 482 cases the ED components (dotted) is limited to the boundary layer and the MF com-
 483 ponent (dashed) dominates above it, as expected.

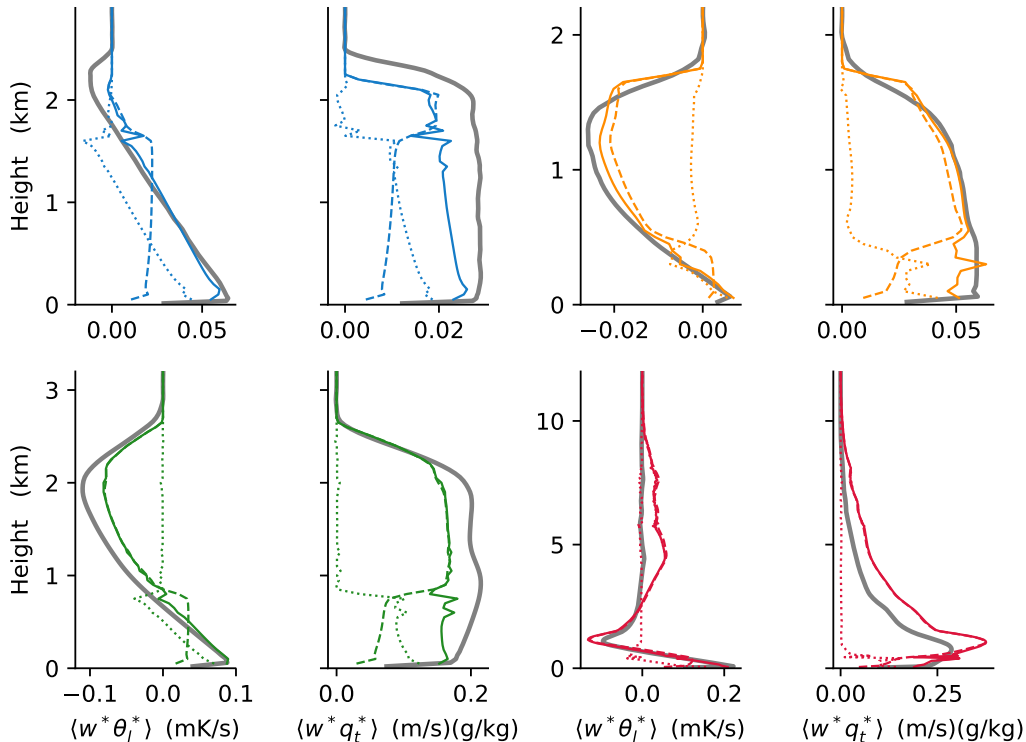


Figure 6. Solid lines show a comparison of the vertical fluxes $\langle w^* \theta_l^* \rangle$ and $\langle w^* q_t^* \rangle$ in the grid with similar color coding of as in Figure 3. Dashed and dotted lines show in addition the SCM diffusive flux (ED) and massflux (MF) components, respectively.

484 The comparison of updraft and cloud properties in Figure 7 shows good agreement
 485 with LES above cloud base. Below cloud base and in the DCBL, large disagreements in
 486 the mass flux and updraft fractions are found. In these dry conditions, the diagnosis of
 487 updrafts in the LES is ambiguous, which contributes to the discrepancies. The good agree-
 488 ment in the vertical fluxes in the boundary layer shown in Figure 6 implies that the net
 489 of ED and MF effects in the SCM captures the LES fluxes well, irrespective of ambigu-
 490 ities of how the flow domain is decomposed into updrafts and environment.

491 Diurnal cycles of shallow and deep convection are shown in Figure 8. The onset
 492 of convection in the SCM is found to be about half an hour delayed compared with the
 493 LES, while cloud top height is in good agreement between the models. In the decay stage
 494 in the ARM-SGP case, the cloud in the SCM shuts off abruptly, unlike the gradual de-
 495 cline in the LES. This may result from the EDMF assumption that neglects variance in
 496 the (single) updraft, which cannot cross cloud base when its buoyancy right below cloud
 497 base is too low. Good agreement is found in the liquid water path (LWP) between the
 498 SCM and the LES in both cases. In the TRMM-LBA case, this agreement includes the
 499 effect of precipitation on the column integrated q_t . The precipitation sink is used to com-

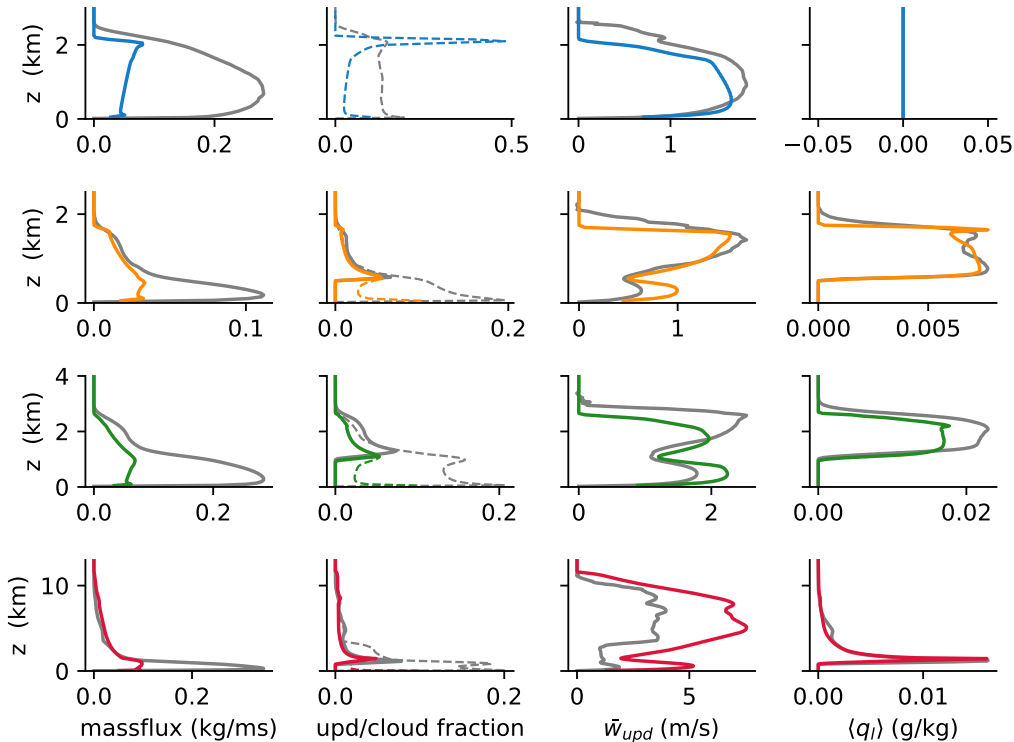


Figure 7. Mean profiles of cloud properties over the last two hours (hours 9-11 in ARM-SGP). Top to bottom rows correspond to DCBL, BOMEX, ARM-SGP, and TRMM-LBA, with SCM following the color-coding in Figure 3 and corresponding LES in gray. Left to right columns correspond to updraft massflux, updraft fraction (dashed) and cloud fraction (solid), updraft vertical velocity and liquid water specific humidity, respectively.

500 pute rain rates in the cutoff microphysics scheme as the vertically integrated amount of
 501 q_t removed at a model time step per unit area. These rain rates show good agreement
 502 with LES counterparts in the TRMM-LBA case in Figure 9.

503 7 Discussions and Conclusions

504 We have presented entrainment and detrainment closures that allow the extended
 505 EDMF scheme to simulate boundary layer turbulence, shallow convection, and deep con-
 506 vection, all within a unified physical framework. The results demonstrate the potential
 507 of the extended EDMF scheme to serve as a unified parameterization for all SGS dynam-
 508 ics in climate models. The choice of parameters used to produce these results is uniform
 509 across all cases and is based on “manual” tuning. We view these results as a proof of con-
 510 cept, which we will now improve further using automated model calibration techniques.

511 The dynamic entrainment/detrainment closures are based on a combination of a
 512 b/w^2 scaling and physically motivated non-dimensional functions, which can in princi-
 513 ple be learnt from data. At the moment, these functions are based on arguments from
 514 buoyancy sorting and relative humidity differences between clouds and their environment.
 515 The addition of turbulent entrainment, which only affects scalars, allows us to regulate
 516 the mass flux by reducing the vertical velocity without increasing the area fraction be-
 517 low cloud base, where detrainment is negligible.

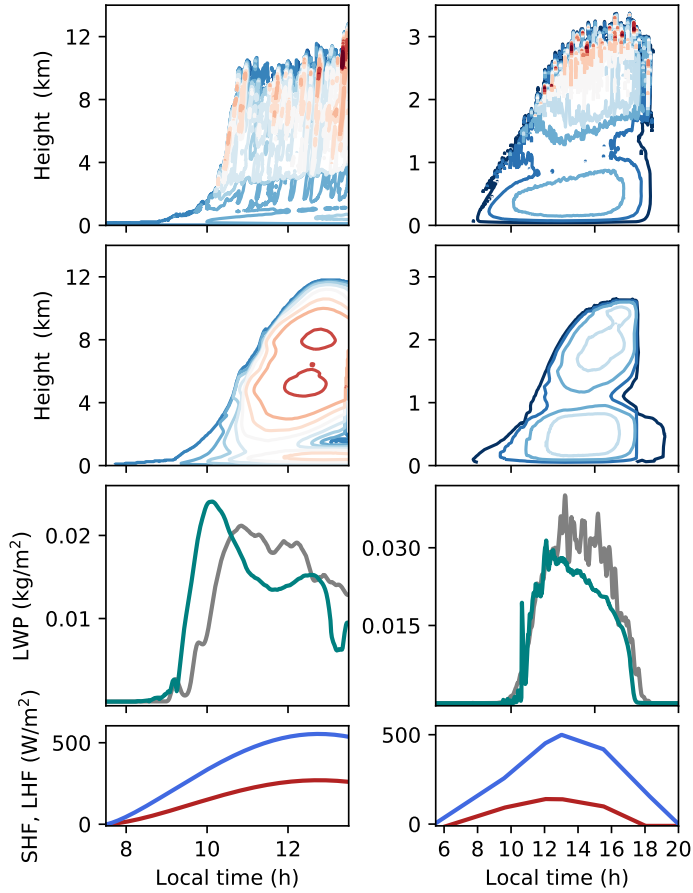


Figure 8. Diurnal cycle in the TRMM-LBA case (left column) and in the ARM-SGP case (right column). Contours show updraft vertical velocity in the LES (first row) and SCM (second row). Contours levels are at $(-2, -1, \dots, 10)$ m s^{-1} for TRMM-LBA and at $(0.5, 0, \dots, 4.5)$ m s^{-1} for ARM-SGP. The third row shows the liquid water path (LWP) in the SCM (green) and LES (gray). The bottom row show the surface latent flux (blue) and sensible heat flux (red).

518 The extended EDMF scheme produces good agreement with LES in key proper-
 519 ties needed for climate modeling. The successful simulation of high-order moments and
 520 vertical fluxes justifies the EDMF assumption of a negligible contribution from updraft
 521 covariance to the grid scale covariance. It would be straightforward to include multiple
 522 updrafts R. A. J. Neggers et al. (2002); R. Neggers (2012); Sušelj et al. (2012), which
 523 can further improve the results. Using multiple updrafts would also open up the oppor-
 524 tunity to include stochastic components either in the updrafts' boundary conditions or
 525 in the entrainment and detrainment closures Sušelj et al. (2013); Suselj et al. (2014); Romps
 526 (2016); Suselj et al. (2019a), with the nonlinearity of the model ensuring that the stochas-
 527 tic effect will not average out in the grid mean.

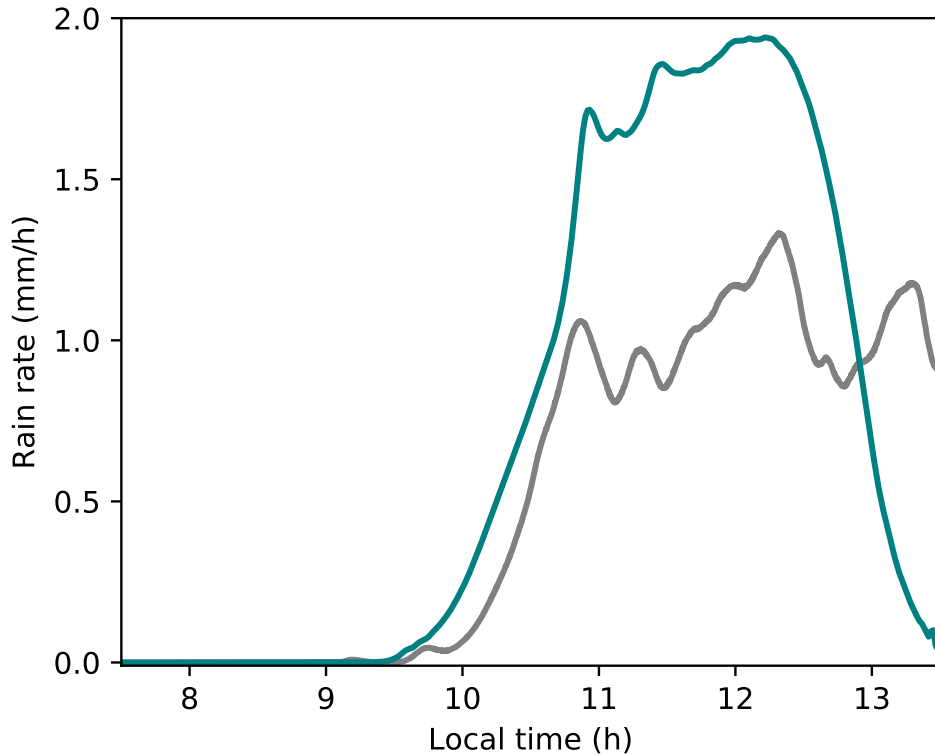


Figure 9. A comparison of the rain rates in the TRMM-LBA case between the SCM (green) and LES (gray).

528 There is a growing interest in using artificial neural networks as SGS models for
 529 turbulence and convection (e.g., Rasp et al., 2018; O’Gorman & Dwyer, 2018). It is worth
 530 noting that the extended EDMF scheme with multiple up- and downdrafts has a net-
 531 work structure: the subdomains play the role of network nodes, which interact through
 532 sigmoidal activation functions (entrainment/detrainment). Each node has memory (ex-
 533 plicitly time-dependent terms), somewhat akin to long short-term memory (LSTM) net-
 534 works (Hochreiter & Schmidhuber, 1997). Unlike artificial neural networks whose archi-
 535 tecture is not tailor-made for the physical problem at hand, the architecture of the ex-
 536 tended EDMF scheme ensures physical realizability and conservation of energy. Like for
 537 neural networks, the activation functions and other parameters in the extended EDMF
 538 scheme can be learnt from data. Our results, which required adjustment of only a hand-
 539 ful of parameters, show that only a small fraction of the data typically required to train
 540 neural networks is needed to calibrate the extended EDMF scheme.

541 The explicitly time-dependent nature of the extended EDMF scheme makes it well
 542 suited to operate across a wide range of GCM resolutions and under time varying large-
 543 scale conditions that may include diurnal cycles and variability on even shorter timescales
 544 (Tan et al., 2018).

Appendix A Computation of Central Second and Third Moments

The second moment of SGS variations is given in terms of the EDMF decomposition by applying the Reynolds decomposition to the product of two scalars,

$$\langle \phi^* \psi^* \rangle = \langle \phi \psi \rangle - \langle \phi \rangle \langle \psi \rangle, \quad (\text{A1})$$

and applying the subdomain decomposition to the first term on right-hand side of (A1):

$$\langle \phi^* \psi^* \rangle = \sum_{i \geq 0} a_i \overline{\phi'_i \psi'_i} + \sum_{i \geq 0} a_i \bar{\phi}_i \bar{\psi}_i - \langle \phi \rangle \langle \psi \rangle. \quad (\text{A2})$$

Multiplying the last term on the right-hand side of (A2) by (8) (which equals unity), the entire right-hand side of this equation yields the first equality in (10). Alternatively, replacing the grid-mean scalars $\langle \psi \rangle$ and $\langle \phi \rangle$ in (A2) by (9) and combining the summations of mean terms yields:

$$\langle \phi^* \psi^* \rangle = \sum_{i \geq 0} a_i \overline{\phi'_i \psi'_i} + \sum_{i \geq 0} \sum_{j \geq 0} a_i a_j \bar{\phi}_i (\bar{\psi}_i - \bar{\psi}_j). \quad (\text{A3})$$

From here, the second equality in (10) is derived by splitting the second summation in (A3) into two identical terms with a factor 1/2, replacing the role of i and j in one of them and summing them back together.

Similarly, the third moment of SGS variations is given by considering the product of three scalars as a single variable,

$$\langle \phi \psi w \rangle = \sum_{i \geq 0} a_i \overline{(\phi \psi w)_i}. \quad (\text{A4})$$

The mean product of three joint scalars can be decomposed as

$$\langle \phi \psi w \rangle = \langle \phi^* \psi^* w^* \rangle + \langle \phi \rangle \langle \psi^* w^* \rangle + \langle \psi \rangle \langle \phi^* w^* \rangle + \langle w \rangle \langle \psi^* \phi^* \rangle + \langle \phi \rangle \langle \psi \rangle \langle w \rangle, \quad (\text{A5})$$

and in the i -th subdomain it is

$$\overline{(\phi \psi w)_i} = \overline{\phi'_i \psi'_i w'_i} + \bar{\phi}_i \overline{\psi'_i w'_i} + \bar{\psi}_i \overline{\phi'_i w'_i} + \bar{w}_i \overline{\psi'_i \phi'_i} + \bar{\phi}_i \bar{\psi}_i \bar{w}_i. \quad (\text{A6})$$

Substituting (A5) and (A6) into (A4) yields (11). Finally, the centered third moment is computed using the domain averages of the scalar, its square, and its cube as

$$\langle \phi^* \phi^* \phi^* \rangle = \langle (\phi - \langle \phi \rangle)^3 \rangle = \langle \phi^3 \rangle - 3\langle \phi \rangle \langle \phi \phi \rangle + 2\langle \phi \rangle^3. \quad (\text{A7})$$

Appendix B Derivation of Subdomain First and Second Moment Equations

Here we derive the prognostic equations for the subdomain area fraction a_i , the subdomain-mean, and the subdomain covariance for any pair of scalars ϕ, ψ . In this derivation, we assume $\rho_i = \langle \rho \rangle$ anywhere but in the buoyancy term, much like in the anelastic model. This ‘‘SGS anelastic’’ assumption removes subgrid-scale sound waves and circumvents the need to define a subdomain pressure (Thuburn et al., 2019). The molecular viscosity and diffusivity are both neglected in the first moment equations, but are reintroduced in the second moment equations in order to account for the dissipation of covariance at the smallest scales.

The subdomain-averaged equations are derived by averaging the governing equations in flux form over the subdomain Ω_i . For scalar ϕ :

$$\int_{\Omega_i(t)} \frac{\partial \rho \phi}{\partial t} dV + \int_{\Omega_i(t)} \nabla \cdot (\rho \phi \mathbf{u}) dV = \int_{\Omega_i(t)} \rho S_\phi dV. \quad (\text{B1})$$

Without loss of generality, the subdomain boundary $\partial\Omega_i$ can be expressed as the union $\partial\Omega_i = \partial\Omega_i^g \cup \partial\Omega_i^{sg}$, where $\partial\Omega_i^g = \partial\Omega_i \cap \partial\Omega_T$ is the common boundary between the grid-box Ω_T and the subdomain Ω_i , which are related through $\sum_i \partial\Omega_i^g = \Omega_T$. The subgrid boundary $\partial\Omega_i^{sg}$ is a free moving surface with velocity \mathbf{u}_b , while boundary $\partial\Omega_i^g$ is fixed. Using the Reynolds transport theorem for the transient term, the Gauss-Ostrogradsky theorem for the divergence, and rearranging the surface integrals yields

$$\frac{\partial}{\partial t} \int_{\Omega_i(t)} \rho\phi dV + \int_{\partial\Omega_i^g} \rho\phi\mathbf{u} \cdot \mathbf{n} dS = - \int_{\partial\Omega_i^{sg}(t)} \rho\phi(\mathbf{u} - \mathbf{u}_b) \cdot \mathbf{n} dS + \int_{\Omega_i(t)} \rho S_\phi dV, \quad (\text{B2})$$

where \mathbf{n} is the outwards pointing unit vector normal to the surface over which the integration is performed. The first term on the right-hand side is the flux out of subdomain Ω_i into other subdomains within the same grid box, and the second term on the left-hand side is the flux out of subdomain Ω_i to a neighboring grid-box. The total grid-scale divergence equals the sum of fluxes from all subdomains across the grid box,

$$\nabla \cdot \int_{\Omega_T} (\rho\phi\mathbf{u}) dV = \int_{\Omega_T} \nabla \cdot (\rho\phi\mathbf{u}) dV = \sum_{i \geq 0} \int_{\partial\Omega_i^g} \rho\phi\mathbf{u} \cdot \mathbf{n} dS, \quad (\text{B3})$$

where the commutativity of the gradient and the volume average is exact for uniform grids and results in a small error otherwise (Fureby & Tabor, 1997). Using the domain decomposition in (9), the leftmost term in (B3) can be written in terms of the sum of the subdomain-mean values,

$$\sum_{i \geq 0} \nabla \cdot [\rho V_i (\overline{\phi\mathbf{u}})_i] = \sum_{i \geq 0} \int_{\partial\Omega_i^g} \rho\phi\mathbf{u} \cdot \mathbf{n} dS, \quad (\text{B4})$$

where V_i is the volume of subdomain Ω_i , and (B4) holds generally. Note that the divergence in (B4) acts on the grid scale. The diagnosis of the contribution of each subdomain to the grid-mean divergence requires an assumption regarding the fraction of $\delta\Omega_T$ covered by each $\delta\Omega_i^g$. Here, we assume that $A_i^g = a_i A_T^g$, where A_i^g and A_T^g are the areas of surfaces $\delta\Omega_i^g$ and $\delta\Omega_T^g$, respectively. We further assume that for each Ω_i the average over $\partial\Omega_i^g$ equals the subdomain mean. From this it follows that

$$\int_{\partial\Omega_i^g} \rho\phi\mathbf{u} \cdot \mathbf{n} dS = \nabla \cdot [\rho V_i (\overline{\phi\mathbf{u}})_i] = \nabla \cdot [\rho V_i (\overline{\phi_i \mathbf{u}_i} + \overline{\phi_i' \mathbf{u}_i'})]. \quad (\text{B5})$$

Note that (B5) cannot be obtained from the divergence theorem, since $\partial\Omega_i^g$ is not a closed surface. Using (B5) and dividing by the grid-box volume V_T , we can rewrite (B2) as

$$\frac{\partial(\rho a_i \overline{\phi_i})}{\partial t} = -\nabla \cdot [\rho a_i (\overline{\phi_i \mathbf{u}_i} + \overline{\phi_i' \mathbf{u}_i'})] - \frac{1}{V_T} \int_{\partial\Omega_i^{sg}(t)} \rho\phi\mathbf{u}_r \cdot \mathbf{n} dS + \rho a_i \overline{S_\phi}, \quad (\text{B6})$$

579 where $\mathbf{u}_r = \mathbf{u} - \mathbf{u}_b$. Since the vertical extent of the volumes is fixed at the model ver-
580 tical resolution, $V_i/V_T = \langle A_i \rangle/A_T = a_i$, with a_i as the area fraction.

The net entrainment flux can be written in terms of a contribution from net mass entrainment and a contribution due to the subfilter-scale flux of ϕ :

$$\frac{1}{V_T} \int_{\partial\Omega_i^{sg}(t)} \rho\phi\mathbf{u}_r \cdot \mathbf{n} dS = \frac{A_{sg}}{V_T} \left(\underbrace{\rho \widehat{\phi u_{r,n}}}_{\text{dynamical}} + \underbrace{\rho \phi' \widehat{u'_{r,n}}}_{\text{turbulent}} \right). \quad (\text{B7})$$

Here, $\widehat{(\cdot)}$ represents the average over interface $\partial\Omega_i^{sg}$, $u_{r,n} = \mathbf{u}_r \cdot \mathbf{n}$, and A_{sg} is the total area of surface $\partial\Omega_i^{sg}$. The two terms on the right-hand side of (B7) are denoted as net dynamical and turbulent entrainment fluxes, respectively. The net dynamical entrainment flux is taken to be the sum of two terms. For mass, it is written as

$$-\frac{A_{sg}}{V_T} (\rho \widehat{u_{r,n}}) = \sum_{j \neq i} (E_{ij} - \Delta_{ij}), \quad (\text{B8})$$

and for a scalar as

$$-\frac{A_{sg}}{V_T}(\rho\widehat{\phi'u_{r,n}}) = \sum_{j \neq i} (E_{ij}\bar{\phi}_j - \Delta_{ij}\bar{\phi}_i), \quad (\text{B9})$$

581 where the entrainment E_{ij} and the detrainment Δ_{ij} are positive semidefinite.

The turbulent entrainment flux does not involve mass exchange between subdomains, and it is modeled as shown in Section 3.2:

$$-\frac{A_{sg}}{V_T}(\rho\phi'u'_{r,n}) = \sum_{j \neq i} \hat{E}_{ij}(\bar{\phi}_j - \bar{\phi}_i). \quad (\text{B10})$$

582 Here, \hat{E}_{ij} is the turbulent entrainment rate from the j -th subdomain into the i -th sub-
 583 domain. Using (B9) and (B10), decomposing the divergence term into vertical and hor-
 584 izontal components, and applying the eddy diffusivity assumption for the vertical tur-
 585 bulent flux, (B6) is written in the form (20). By setting $\phi = 1$ in (20), the mass con-
 586 tinuity (i.e., area fraction) equation (18) follows.

The second-moment equations can be derived by first writing (B6) for the product of two scalars $\phi\psi$. Using (B7), and decomposing the divergence term into vertical and horizontal components, we obtain

$$\begin{aligned} \frac{\partial(\rho a_i \overline{\phi_i \psi_i})}{\partial t} + \nabla_h \cdot (\rho a_i \langle \mathbf{u}_h \rangle \overline{\phi_i \psi_i}) + \frac{\partial(\rho a_i \overline{\phi_i \psi_i \bar{w}_i})}{\partial z} + \frac{\partial(\rho a_i (\overline{\phi_i \psi_i})' w'_i)}{\partial z} = \\ - \frac{A_{sg}}{V_T} (\rho \widehat{\phi\psi} u'_{r,n} + \rho (\phi\psi)' u'_{r,n}) + \rho a_i \overline{S_{\phi\psi,i}}. \end{aligned} \quad (\text{B11})$$

The subdomain covariance equation can then be obtained from (20), (18), and (B11) as

$$\frac{\partial(\rho a_i \overline{\phi'_i \psi'_i})}{\partial t} = \frac{\partial(\rho a_i \overline{\phi_i \psi_i})}{\partial t} - \bar{\psi}_i \frac{\partial(\rho a_i \bar{\phi}_i)}{\partial t} - \bar{\phi}_i \frac{\partial(\rho a_i \bar{\psi}_i)}{\partial t} + \bar{\phi}_i \bar{\psi}_i \frac{\partial(\rho a_i)}{\partial t}, \quad (\text{B12})$$

which leads to

$$\begin{aligned} \frac{\partial(\rho a_i \overline{\phi'_i \psi'_i})}{\partial t} + \nabla_h \cdot (\rho a_i \langle \mathbf{u}_h \rangle \overline{\phi'_i \psi'_i}) + \frac{\partial(\rho a_i \bar{w}_i \overline{\phi'_i \psi'_i})}{\partial z} = \\ \frac{\partial(\rho a_i \overline{w'_i \phi'_i \psi'_i})}{\partial z} - \rho a_i \overline{w'_i \phi'_i} \frac{\partial \bar{\psi}_i}{\partial z} - \rho a_i \overline{w'_i \psi'_i} \frac{\partial \bar{\phi}_i}{\partial z} - \rho \frac{A_{sg}}{V_T} (\phi' \psi' u'_{r,n} - (\bar{\psi}_i - \hat{\psi}) u'_{r,n} \phi' - (\bar{\phi}_i - \hat{\phi}) u'_{r,n} \psi') \\ - \rho \frac{A_{sg}}{V_T} (\hat{u}_{r,n} (\hat{\phi} - \bar{\phi}_i) (\hat{\psi} - \bar{\psi}_i) + \hat{u}_{r,n} \phi' \psi') - \rho a_i \overline{D_{\phi'\psi',i}} + \rho a_i (\overline{S'_{\phi,i} \psi'} + \overline{S'_{\psi,i} \phi'}). \end{aligned} \quad (\text{B13})$$

Here, terms of the form $(\bar{\psi}_i - \hat{\psi}) u'_{r,n} \phi'$ are written as $\bar{\psi}_i^* u'_{r,n} \phi'$ to ensure conservation of second moments on the host model grid. The last term in (B13) follows from (B12), given that

$$\overline{S_{\phi\psi,i}} = \bar{\phi}_i \overline{S_{\psi,i}} + \bar{\psi}_i \overline{S_{\phi,i}}. \quad (\text{B14})$$

The dissipation of covariance is represented by $\overline{D_{\phi'\psi',i}}$. The vertical subgrid covariance flux is written as downgradient and proportional to the eddy diffusivity $K_{\phi\psi,i}$:

$$\frac{\partial(\rho a_i \overline{w'_i \phi'_i \psi'_i})}{\partial z} = - \frac{\partial}{\partial z} \left[\rho a_i K_{\phi\psi,i} \frac{\partial}{\partial z} (\overline{\phi'_i \psi'_i}) \right]. \quad (\text{B15})$$

587 Substituting (B9), (B10), and (B15) in (B13) we obtain (22). The extended EDMF
 588 scheme only makes use of covariance equations for thermodynamic variables θ_l and q_t
 589 and for the turbulence kinetic energy. Subgrid-scale covariances between thermodynamic
 590 variable and momentum are modeled diffusively following (14).

591
 592

Appendix C Energy conserving form of the SGS anelastic approximation

The SGS anelastic approximation amounts to assuming $\bar{\rho}_i = \langle \rho \rangle$ everywhere except in the gravity term in the vertical momentum equation. Following Pauluis (2008), the energy-conserving form for the SGS anelastic approximation can be derived from a linear expansion of the density about its grid-mean value, considering independently the changes with respect to pressure and with respect to temperature and humidity. Linearizing the density about $\langle \rho \rangle$, we write:

$$\bar{\rho}_i(\bar{\theta}_{l,i}, \bar{q}_{t,i}, \bar{p}_i) = \langle \rho \rangle + \delta \bar{\rho}_i(\bar{\theta}_{l,i}, \bar{q}_{t,i}, \langle p \rangle) + \left(\frac{\partial \rho}{\partial p} \right)_{\theta_i, q_t} (\bar{p}_i - \langle p \rangle). \quad (\text{C1})$$

Substituting (C1) in (15), the subdomain buoyancy is written as

$$\bar{b}_i = \underbrace{-g \frac{\delta \bar{\rho}_i + \langle \rho \rangle - \rho_h}{\langle \rho \rangle}}_{\approx \bar{b}_i} - \underbrace{\frac{g}{\langle \rho \rangle} \left(\frac{\partial \rho}{\partial p} \right)_{\theta_i, q_t}}_{\text{SGS sound-waves}} (\bar{p}_i - \langle p \rangle). \quad (\text{C2})$$

By using the first term on the right-hand side as the effective subdomain buoyancy, the SGS sound waves represented by the second term are neglected. The subdomain perturbation pressure gradient is written using the SGS anelastic approximation as

$$-\frac{1}{\langle \rho \rangle} \frac{\partial \bar{p}_i^\dagger}{\partial z} = -\frac{\partial}{\partial z} \left(\frac{\bar{p}_i^\dagger}{\langle \rho \rangle} \right) - \frac{\bar{p}_i^\dagger}{\langle \rho \rangle^2} \frac{\partial \langle \rho \rangle}{\partial z} = -\frac{\partial}{\partial z} \left(\frac{\bar{p}_i^\dagger}{\langle \rho \rangle} \right) - \frac{\bar{p}_i^\dagger}{\langle \rho \rangle^2} \frac{\partial \langle \rho \rangle}{\partial p_h} \frac{\partial p_h}{\partial z}. \quad (\text{C3})$$

An energy conserving form of this ‘‘SGS anelastic’’ approximation (i.e., with $\langle \rho \rangle$ inside the pressure gradient term) is obtained by a mutual cancellation between the last terms on the right-hand sides of (C3) and (C2). This cancellation of terms is obtained by applying the hydrostatic balance and assuming

$$\frac{\bar{p}_i - \langle p \rangle}{\rho_h} \left(\frac{\partial \rho}{\partial p} \right)_{\theta_i, q_t} \approx \frac{\bar{p}_i - p_h}{\langle \rho \rangle} \frac{\partial \langle \rho \rangle}{\partial p_h}.$$

 593
 594
 595
 596
 597

This derivation differs from that in Pauluis (2008) by the fact that the grid-mean values are not necessarily hydrostatic. By setting the grid-mean value to the reference value for both pressure and density, equation (6) in Pauluis (2008) is recovered. Using these assumptions in the subdomain vertical velocity equation provides the justification for the energy conserving form of the pressure term in (19).

598

Appendix D Entrainment and Detrainment diagnosis from LES

The direct estimation of entrainment and detrainment is based on calculating $\epsilon - \delta$ from (18), while $\epsilon + \hat{\epsilon}$ can be independently estimated from the advective form of the equation for $\bar{q}_{t,i}$,

$$\frac{\partial \bar{q}_{t,i}}{\partial t} + \bar{w}_i \frac{\partial \bar{q}_{t,i}}{\partial z} + \frac{1}{\rho a_i} \frac{\partial (\rho a_i \overline{w'_i q'_{t,i}})}{\partial z} = \bar{w}_i \sum_{j \neq i} (\epsilon_{ij} + \hat{\epsilon}_{ij}) (\bar{q}_{t,j} - \bar{q}_{t,i}) + S_{\bar{q}_{t,i}}. \quad (\text{D1})$$

When considering the decomposition into one updraft and its environment, this reduces to

$$\epsilon_{i0} + \hat{\epsilon}_{i0} = \frac{1}{\bar{w}_i (\bar{q}_{t,0} - \bar{q}_{t,i})} \left(\frac{\partial \bar{q}_{t,i}}{\partial t} + \bar{w}_i \frac{\partial \bar{q}_{t,i}}{\partial z} + \frac{1}{\bar{\rho}_i a_i} \frac{\partial (\bar{\rho}_i a_i \overline{w'_i q'_{t,i}})}{\partial z} - S_{\bar{q}_{t,i}} \right). \quad (\text{D2})$$

 599
 600
 601
 602

Note that the vertical turbulent flux is added in this diagnostic equation for the updrafts, even though it is neglected in updrafts in the EDMF scheme. It was found that without this vertical turbulent flux in the diagnosis, the estimated ϵ_{i0} is much more likely to result in unphysical (i.e., negative) values.

603 **Appendix E Derivation of entrainment function from conditions on**
 604 **the mass-flux and velocity ratio at cloud top**

The vertical mass flux is defined as $\rho a_i \bar{w}_i$. As $z \rightarrow z_{\text{top}}$, the height at which the area fraction vanishes, the ratio between the mass-flux and the vertical velocity should be maintained:

$$\lim_{z \rightarrow z_{\text{top}}} \left[\frac{\rho a_i \bar{w}_i}{\bar{w}_i} \right] = \lim_{z \rightarrow z_{\text{top}}} \left[\frac{\partial(\rho a_i \bar{w}_i) / \partial z}{\partial \bar{w}_i / \partial z} \right] = \rho a_i. \quad (\text{E1})$$

Here, we used L'Hopital's rule. Using the steady form of (18) in the numerator and the advective form of (19) in the denominator, we obtain:

$$\lim_{z \rightarrow z_{\text{top}}} \left[\frac{\rho a_i \bar{w}_i (\epsilon_{i0} - \delta_{i0})}{[\bar{b}_i - \partial(\bar{p}_i^\dagger / \rho) / \partial z] / \bar{w}_i - (\epsilon_{i0} + \hat{\epsilon}_{i0})(\bar{w}_i - \bar{w}_0)} \right] = \rho a_i, \quad (\text{E2})$$

where the turbulent transport inside the updraft has been neglected. This equation implies:

$$\delta_{i0} = \epsilon_{i0} \left(2 - \frac{\bar{w}_0}{\bar{w}_i} \right) + \hat{\epsilon}_{i0} \left(1 - \frac{\bar{w}_0}{\bar{w}_i} \right) - \frac{1}{\bar{w}_i^2} \left[\bar{b}_i - \frac{\partial}{\partial z} \left(\frac{\bar{p}_i^\dagger}{\rho} \right) \right]. \quad (\text{E3})$$

605 If we further assume that in this limit, $\epsilon + \hat{\epsilon} \ll \delta$, the above equation provides a func-
 606 tional form for δ similar to that obtained by Roms (2016).

607 **Acknowledgments**

608 This research was made possible by the generosity of Eric and Wendy Schmidt by rec-
 609 ommendation of the Schmidt Futures program, by Earthrise Alliance, Mountain Philan-
 610 thropies, the Paul G. Allen Family Foundation, and the National Science Foundation (NSF,
 611 award AGS-1835860). I.L. was additionally supported by a Resnick Sustainability Fel-
 612 lowship. Parts of the research were carried out at the Jet Propulsion Laboratory, Cal-
 613 ifornia Institute of Technology, under a contract with the National Aeronautics and Space
 614 Administration (80NM0018D0004) and funded through the internal Research and Tech-
 615 nology Development program.

616 © 2020. California Institute of Technology. Government sponsorship acknowledged.

617 **References**

- 618 Asai, T., & Kasahara, A. (1967). A theoretical study of the compensating downward
 619 motions associated with cumulus clouds. *Journal of the Atmospheric Sciences*,
 620 *24*(5), 487–496. doi: 10.1175/1520-0469(1967)024<0487:ATSOTC>2.0.CO;2
- 621 Bechtold, P., Köhler, M., Jung, T., Doblas-Reyes, F., Leutbecher, M., Rodwell,
 622 M. J., ... Balsamo, G. (2008). Advances in simulating atmospheric variabil-
 623 ity with the ECMWF model: From synoptic to decadal time-scales. *Quar-*
 624 *terly Journal of the Royal Meteorological Society*, *134*(634), 1337–1351. doi:
 625 10.1002/qj.289
- 626 Bechtold, P., Semane, N., Lopez, P., Chaboureau, J.-P., Beljaars, A., & Bormann,
 627 N. (2014). Representing equilibrium and nonequilibrium convection in large-
 628 scale models. *Journal of the Atmospheric Sciences*, *71*(2), 734–753. doi:
 629 10.1175/JAS-D-13-0163.1
- 630 Böing, S., Siebesma, A., Korpershoek, J., & Jonker, H. J. (2012). Detrain-
 631 ment in deep convection. *Geophysical Research Letters*, *39*(20). doi:
 632 10.1029/2012GL053735
- 633 Bony, S., & Dufresne, J.-L. (2005). Marine boundary layer clouds at the heart of
 634 tropical cloud feedback uncertainties in climate models. *Geophysical Research*
 635 *Letters*, *32*(20). doi: 10.1029/2005GL023851

- 636 Bretherton, C. S., McCaa, J. R., & Grenier, H. (2004). A new parameterization
637 for shallow cumulus convection and its application to marine subtropical
638 cloud-topped boundary layers. part i: Description and 1d results. *Monthly*
639 *Weather Review*, *132*(4), 864–882. doi: /10.1175/1520-0493(2004)132<0864:
640 ANPFSC>2.0.CO;2
- 641 Brient, F., & Schneider, T. (2016). Constraints on climate sensitivity from space-
642 based measurements of low-cloud reflection. *Journal of Climate*, *29*, 5821–
643 5835. doi: /10.1175/JCLI-D-15-0897.1
- 644 Brient, F., Schneider, T., Tan, Z., Bony, S., Qu, X., & Hall, A. (2016). Shallowness
645 of tropical low clouds as a predictor of climate models’ response to warming.
646 *Climate Dynamics*, *47*, 433–449. doi: 10.1007/s00382-015-2846-0
- 647 Brown, A., Cederwall, R., Chlond, A., Duynkerke, P., Golaz, J.-C., Khairoutdi-
648 nov, M., . . . others (2002). Large-eddy simulation of the diurnal cycle of
649 shallow cumulus convection over land. *Quarterly Journal of the Royal Me-*
650 *teorological Society*, *128*(582), 1075–1093. doi: https://doi.org/10.1256/
651 003590002320373210
- 652 Caldwell, P. M., Zelinka, M. D., & Klein, S. A. (2018). Evaluating emergent con-
653 straints on equilibrium climate sensitivity. *Journal of Climate*, *31*, 3921–3942.
654 doi: 10.1175/JCLI-D-17-0631.1
- 655 Ceppi, P., Brient, F., Zelinka, M. D., & Hartmann, D. L. (2017). Cloud feedback
656 mechanisms and their representation in global climate models. *Wiley Interdis-*
657 *ciplinary Reviews: Climate Change*, *e465*. doi: 10.1002/wcc.465
- 658 Cesana, G., Del Genio, A. D., & Ackerman, A. (n.d.). Constraining the models’ re-
659 sponse of tropical clouds to sst forcings using calipso observations. In *Remote*
660 *sensing and modeling of the atmosphere, oceans, and interactions vii*.
- 661 Couvreux, F., Hourdin, F., & Rio, C. (2010). Resolved versus parametrized
662 boundary-layer plumes. part i: A parametrization-oriented conditional sam-
663 pling in large-eddy simulations. *Boundary-Layer Meteorology*, *134*(3), 441–458.
664 doi: 10.1007/s10546-009-9456-5
- 665 de Rooy, W. C., Bechtold, P., Fröhlich, K., Hohenegger, C., Jonker, H., Mironov,
666 D., & et al. (2013). Entrainment and detrainment in cumulus convection: An
667 overview. *Quarterly Journal of the Royal Meteorological Society*, *139*, 1–19.
668 doi: 10.1002/qj.1959
- 669 de Rooy, W. C., & Siebesma, P. A. (2010). Analytical expressions for entrainment
670 and detrainment in cumulus convection. *Quarterly Journal of the Royal Meteo-*
671 *rological Society*, *136*(650), 1216–1227. doi: /10.1002/qj.640
- 672 Dirmeyer, P. A., Cash, B. A., Kinter, J. L., Jung, T., Marx, L., Satoh, M., . . . Man-
673 ganello, J. (2012). Simulating the diurnal cycle of rainfall in global climate
674 models: Resolution versus parameterization. *Climate Dynamics*, *39*(1-2),
675 399–418. doi: 10.1007/s00382-011-1127-9
- 676 Dong, Y., Proistosescu, C., Armour, K. C., & Battisti, D. S. (2019). Attributing
677 historical and future evolution of radiative feedbacks to regional warming pat-
678 terns using a green’s function approach: The preeminence of the western pa-
679 cific. *Journal of Climate*, *32*(17), 5471–5491. doi: 10.1175/JCLI-D-18-0843.1
- 680 Fureby, C., & Tabor, G. (1997). Mathematical and physical constraints on large-
681 eddy simulations. *Theoretical and Computational Fluid Dynamics*, *9*(2), 85–
682 102. doi: 10.1007/s001620050034
- 683 Gao, Y., Leung, L. R., Zhao, C., & Hagos, S. (2017). Sensitivity of us summer
684 precipitation to model resolution and convective parameterizations across gray
685 zone resolutions. *Journal of Geophysical Research: Atmospheres*, *122*(5),
686 2714–2733. doi: 10.1002/2016JD025896
- 687 Golaz, J.-C., Larson, V. E., & Cotton, W. R. (2002). A pdf-based model for bound-
688 ary layer clouds. part I: Method and model description. *Journal of the Atmo-*
689 *spheric Sciences*, *59*(24), 3540–3551. doi: 10.1175/1520-0469(2002)059<3540:
690 APBMFB>2.0.CO;2

- 691 Grabowski, W., Bechtold, P., Cheng, A., Forbes, R., Halliwell, C., Khairoutdinov,
692 M., ... et al. (2006). Daytime convective development over land: A model
693 intercomparison based on Iba observations. *Quarterly Journal of the Royal*
694 *Meteorological Society*, 132(615), 317–344. doi: doi.org/10.1256/qj.04.147
- 695 Gregory, D. (2001). Estimation of entrainment rate in simple models of convective
696 clouds. *Quarterly Journal of the Royal Meteorological Society*, 127, 53–72. doi:
697 10.1002/qj.49712757104
- 698 Han, J., & Bretherton, C. S. (2019). Tke-based moist eddy-diffusivity mass-flux
699 (edmf) parameterization for vertical turbulent mixing. *Weather and Forecast-*
700 *ing*, 34(4), 869–886. doi: 10.1175/WAF-D-18-0146.1
- 701 Hirota, N., Takayabu, Y. N., Watanabe, M., Kimoto, M., & Chikira, M. (2014). Role
702 of convective entrainment in spatial distributions of and temporal variations in
703 precipitation over tropical oceans. *Journal of Climate*, 27(23), 8707–8723. doi:
704 /10.1175/JCLI-D-13-00701.1
- 705 Hochreiter, S., & Schmidhuber, J. (1997). Long short-term memory. *Neural compu-*
706 *tation*, 9(8), 1735–1780. doi: 10.1162/neco.1997.9.8.1735
- 707 Holland, J. Z., & Rasmusson, E. M. (1973). Measurements of the atmospheric
708 mass, energy, and momentum budgets over a 500-kilometer square of trop-
709 ical ocean. *Monthly Weather Review*, 101(1), 44–57. doi: 10.1175/
710 1520-0493(1973)101<0044:MOTAME>2.3.CO;2
- 711 Holtslag, A., Svensson, G., Baas, P., Basu, S., Beare, B., Beljaars, A., & et al.
712 (2013). Stable atmospheric boundary layers and diurnal cycles: Challenges
713 for weather and climate models. *Bulletin of the American Meteorological*
714 *Society*, 94(11), 1691–1706. doi: 10.1175/BAMS-D-11-00187.1
- 715 Hourdin, F., Mauritsen, T., Gettelman, A., Golaz, J.-C., Balaji, V., Duan, Q.,
716 ... Williamson, D. (2017). The art and science of climate model tun-
717 ing. *Bulletin of the American Meteorological Society*, 98, 589–602. doi:
718 BAMS-D-15-00135.1
- 719 Kain, J. S. (2004). The Kain–Fritsch convective parameterization: an up-
720 date. *Journal of Applied Meteorology*, 43(1), 170–181. doi: 10.1175/
721 1520-0450(2004)043<0170:TKCPAU>2.0.CO;2
- 722 Kain, J. S., & Fritsch, J. M. (1990). A one-dimensional entraining/detraining plume
723 model and its application in convective parameterization. *Journal of the Atmo-*
724 *spheric Sciences*, 47(23), 2784–2802. doi: 10.1175/1520-0469(1990)047<2784:
725 AODEPM>2.0.CO;2
- 726 Kajikawa, Y., Miyamoto, Y., Yoshida, R., Yamaura, T., Yashiro, H., & Tomita,
727 H. (2016). Resolution dependence of deep convections in a global simulation
728 from over 10-kilometer to sub-kilometer grid spacing. *Progress in Earth and*
729 *Planetary Science*, 3(1), 16. doi: 10.1186/s40645-016-0094-5
- 730 Kuo, H. (1962). On the controlling influences of eddy diffusion on thermal convec-
731 tion. *Journal of the Atmospheric Sciences*, 19(3), 236–243. doi: 10.1175/1520-
732 -0469(1962)019<0236:OTCIOE>2.0.CO;2
- 733 Langhans, W., Mueller, J., & Collins, W. D. (2019). Optimization of the eddy-
734 diffusivity/mass-flux shallow cumulus and boundary-layer parameterization
735 using surrogate models. *Journal of Advances in Modeling Earth Systems*,
736 11(2), 402–416. doi: 10.1029/2018MS001449
- 737 Lappen, C.-L., & Randall, D. A. (2001a). Toward a unified parameterization
738 of the boundary layer and moist convection. part I: A new type of mass-
739 flux model. *Journal of the Atmospheric Sciences*, 58(15), 2021–2036. doi:
740 10.1175/1520-0469(2001)058<2037:TAUPOT>2.0.CO;2
- 741 Lappen, C.-L., & Randall, D. A. (2001b). Toward a unified parameterization of
742 the boundary layer and moist convection. part II: Lateral mass exchanges and
743 subplume-scale fluxes. *Journal of the Atmospheric Sciences*, 58(15), 2037–
744 2051. doi: 10.1175/1520-0469(2001)058<2037:TAUPOT>2.0.CO;2
- 745 Larson, V. E., Domke, S., & Griffin, B. M. (2019). Momentum transport in shal-

- low cumulus clouds and its parameterization by higher-order closure. *Journal of Advances in Modeling Earth Systems*. doi: 10.1029/2019MS001743
- Larson, V. E., & Golaz, J.-C. (2005). Using probability density functions to derive consistent closure relationships among higher-order moments. *Monthly Weather Review*, *133*(4), 1023–1042. doi: 10.1175/MWR2902.1
- Larson, V. E., Schanen, D. P., Wang, M., Ovchinnikov, M., & Ghan, S. (2012). Pdf parameterization of boundary layer clouds in models with horizontal grid spacings from 2 to 16 km. *Monthly Weather Review*, *140*(1), 285–306. doi: 10.1175/MWR-D-10-05059.1
- Lin, J.-L., Qian, T., & Shinoda, T. (2014). Stratocumulus clouds in southeastern pacific simulated by eight CMIP5–CFMIP global climate models. *Journal of Climate*, *27*(8), 3000–3022. doi: 10.1175/JCLI-D-13-00376.1
- Lopez-Gomez, I., Cohen, Y., He, J., Jaruga, A., & Schneider, T. (2020). A generalized mixing length closure for eddy-diffusivity mass-flux schemes of turbulence and convection. *Preprint on <https://essoar.org>*. doi: 10.1002/essoar.10502906.1
- Mardia, K. V., Kent, J. T., & Bibby, J. M. (1979). *Multivariate analysis*. San Diego, CA: Academic Press.
- McKim, B., Jeevanjee, N., & Lecoanet, D. (2020). Buoyancy-driven entrainment in dry thermals. *Quarterly Journal of the Royal Meteorological Society*, *146*(726), 415–425. doi: 10.1002/qj.3683
- Morton, B., Taylor, G. I., & Turner, J. S. (1956). Turbulent gravitational convection from maintained and instantaneous sources. *Proceedings of the Royal Society of London. Series A. Mathematical and Physical Sciences*, *234*(1196), 1–23. doi: 10.1098/rspa.1956.0011
- Nam, C., Bony, S., Dufresne, J.-L., & Chepfer, H. (2012). The ‘too few, too bright’ tropical low-cloud problem in CMIP5 models. *Geophysical Research Letters*, *39*(21). doi: 10.1029/2012GL053421
- Neggers, R. (2012). Humidity-convection feedbacks in a mass flux scheme based on resolved size densities. In *ECMWF Workshop on Parametrization of Clouds and Precipitation*.
- Neggers, R. A., Neelin, J. D., & Stevens, B. (2007). Impact mechanisms of shallow cumulus convection on tropical climate dynamics. *Journal of Climate*, *20*(11), 2623–2642. doi: 10.1175/JCLI4079.1
- Neggers, R. A. J., Siebesma, A. P., & Jonker, H. J. J. (2002). A multiparcel model for shallow cumulus convection. *Journal of the Atmospheric Sciences*, *59*(10), 1655–1668. doi: 10.1175/1520-0469(2002)059<1655:AMMFSC>2.0.CO;2
- O’Gorman, P. A., & Dwyer, J. G. (2018). Using machine learning to parameterize moist convection: Potential for modeling of climate, climate change, and extreme events. *Journal of Advances in Modeling Earth Systems*, *10*(10), 2548–2563. doi: 10.1029/2018MS001351
- Park, S. (2014a). A unified convection scheme (UNICON). Part I: Formulation. *Journal of the Atmospheric Sciences*, *71*(11), 3902–3930. doi: 10.1175/JAS-D-13-0233.1
- Park, S. (2014b). A unified convection scheme (UNICON). Part II: Simulation. *Journal of the Atmospheric Sciences*, *71*(11), 3931–3973. doi: 10.1175/JAS-D-13-0234.1
- Pauluis, O. (2008). Thermodynamic consistency of the anelastic approximation for a moist atmosphere. *Journal of the Atmospheric Sciences*, *65*(8), 2719–2729. doi: 10.1175/2007JAS2475.1
- Pressel, K. G., Kaul, C. M., Schneider, T., Tan, Z., & Mishra, S. (2015). Large-eddy simulation in an anelastic framework with closed water and entropy balances. *Journal of Advances in Modeling Earth Systems*, *7*(3), 1425–1456. doi: 10.1002/2015MS000496.
- Pressel, K. G., Mishra, S., Schneider, T., Kaul, C. M., & Tan, Z. (2017). Numer-

- 801 ics and subgrid-scale modeling in large eddy simulations of stratocumulus
802 clouds. *Journal of Advances in Modeling Earth Systems*, 9(2), 1342–1365. doi:
803 10.1002/2016MS000778
- 804 Rasp, S., Pritchard, M. S., & Gentine, P. (2018). Deep learning to represent subgrid
805 processes in climate models. *Proceedings of the National Academy of Sciences*,
806 115(39), 9684–9689. doi: 10.1073/pnas.1810286115
- 807 Raymond, D. J., & Blyth, A. M. (1986). A stochastic mixing model for non-
808 precipitating cumulus clouds. *Journal of the Atmospheric Sciences*, 43(22),
809 2708–2718. doi: 10.1175/1520-0469(1986)043<2708:ASMMFN>2.0.CO;2
- 810 Rio, C., Del Genio, A. D., & Hourdin, F. (2019). Ongoing breakthroughs in convective
811 parameterization. *Current Climate Change Reports*, 5(2), 95–111. doi: /
812 10.1007/s40641-019-00127-w
- 813 Romps, D. M. (2008). The dry-entropy budget of a moist atmosphere. *Journal of*
814 *the Atmospheric Sciences*, 65, 3779–3799. doi: 10.1175/2008JAS2679.1
- 815 Romps, D. M. (2016). The stochastic parcel model: A deterministic parameteriza-
816 tion of stochastically entraining convection. *Journal of Advances in Modeling*
817 *Earth Systems*, 8, 319–344. doi: 10.1002/2015MS000537
- 818 Savre, J., & Herzog, M. (2019). A general description of entrainment in buoyant
819 cloudy plumes including the effects of mixing-induced evaporation. *Journal of*
820 *the Atmospheric Sciences*, 76(2), 479–496. doi: 10.1175/JAS-D-17-0326.1
- 821 Schmidt, G. A., Bader, D., Donner, L. J., Elsaesser, G. S., Golaz, J.-C., Hannay, C.,
822 ... Saha, S. (2017). Practice and philosophy of climate model tuning across
823 six u.s. modeling centers. *Geoscientific Model Development*, 10, 3207–3223.
824 doi: 10.5194/gmd-10-3207-2017
- 825 Schneider, T., Kaul, C. M., & Pressel, K. G. (2019). Possible climate transitions
826 from breakup of stratocumulus decks under greenhouse warming. *Nature Geo-*
827 *science*, 12(3), 163. doi: 10.1038/s41561-019-0310-1
- 828 Schneider, T., Teixeira, J., Bretherton, C. S., Brient, F., Pressel, K. G., Schär, C.,
829 & Siebesma, A. P. (2017). Climate goals and computing the future of clouds.
830 *Nature Climate Change*, 7, 3–5. doi: 10.1038/nclimate3190
- 831 Siebesma, A., & Cuijpers, J. (1995). Evaluation of parametric assumptions for shal-
832 low cumulus convection. *Journal of the Atmospheric Sciences*, 52(6), 650–666.
833 doi: 10.1175/1520-0469(1995)052<0650:EOPAFS>2.0.CO;2
- 834 Siebesma, A. P., Bretherton, C. S., Brown, A., Chlond, A., Cuxart, J., Duynkerke,
835 P. G., ... et al. (2003). A large eddy simulation intercomparison study of
836 shallow cumulus convection. *Journal of the Atmospheric Sciences*, 60(10),
837 1201–1219. doi: 10.1175/1520-0469(2003)60<1201:ALESIS>2.0.CO;2
- 838 Siebesma, A. P., Soares, P. M. M., & Teixeira, J. (2007). A combined eddy-
839 diffusivity mass-flux approach for the convective boundary layer. *Journal*
840 *of the Atmospheric Sciences*, 64, 1230–1248. doi: 10.1175/JAS3888.1
- 841 Siebesma, A. P., & Teixeira, J. (2000). An advection-diffusion scheme for the con-
842 vective boundary layer: Description and 1D results [Conference Proceedings].
843 In *American Meteorological Society, 14th Symposium on Boundary Layers and*
844 *Turbulence* (pp. 133–136).
- 845 Soares, P., Miranda, P., Siebesma, A., & Teixeira, J. (2004). An eddy-
846 diffusivity/mass-flux parametrization for dry and shallow cumulus convection.
847 *Quarterly Journal of the Royal Meteorological Society*, 130(604), 3365–3383.
848 doi: 10.1256/qj.03.223
- 849 Stevens, B., Satoh, M., Auger, L., Biercamp, J., Bretherton, C. S., Chen, X., ...
850 Zhou, L. (2019). DYAMOND: the DYNAMics of the Atmospheric general circula-
851 tion Modeled on Non-hydrostatic Domains. *Progress in Earth and Planetary*
852 *Science*, 6, 61. doi: 10.1186/s40645-019-0304-z
- 853 Suselj, K., Hogan, T. F., & Teixeira, J. (2014). Implementation of a stochas-
854 tic eddy-diffusivity/mass-flux parameterization into the Navy Global En-
855 vironmental Model. *Weather and Forecasting*, 29, 1374–1390. doi:

- 10.1175/WAF-D-14-00043.1
- 856
857 Suselj, K., Kurowski, M. J., & Teixeira, J. (2019a). On the factors controlling the
858 development of shallow convection in eddy-diffusivity/mass-flux models. *Journal of the Atmospheric Sciences*, *76*(2), 433–456. doi: 10.1175/JAS-D-18-0121
859 .1
- 860
861 Suselj, K., Kurowski, M. J., & Teixeira, J. (2019b). A unified eddy-diffusivity/mass-
862 flux approach for modeling atmospheric convection. *Journal of the Atmo-
863 spheric Sciences*, *76*(8), 2505–2537. doi: 10.1175/JAS-D-18-0239.1
- 864 Sušelj, K., Teixeira, J., & Chung, D. (2013). A unified model for moist convective
865 boundary layers based on a stochastic eddy-diffusivity/mass-flux parame-
866 terization. *Journal of the Atmospheric Sciences*, *70*(7), 1929–1953. doi:
867 10.1175/JAS-D-12-0106.1
- 868 Sušelj, K., Teixeira, J., & Matheou, G. (2012). Eddy diffusivity/mass flux and shal-
869 low cumulus boundary layer: An updraft pdf multiple mass flux scheme. *Jour-
870 nal of the Atmospheric Sciences*, *69*(5), 1513–1533. doi: 10.1175/JAS-D-11-090
871 .1
- 872 Tan, Z., Kaul, C. M., Pressel, K. G., Cohen, Y., Schneider, T., & Teixeira, J. (2018).
873 An extended eddy-diffusivity mass-flux scheme for unified representation of
874 subgrid-scale turbulence and convection. *Journal of Advances in Modeling
875 Earth Systems*, *10*, 770–800. doi: 10.1002/2017MS001162
- 876 Teixeira, J., Cardoso, S., Bonazzola, M., Cole, J., DelGenio, A., DeMott, C.,
877 & et al. (2011). Tropical and subtropical cloud transitions in weather
878 and climate prediction models: The GCSS/WGNE pacific cross-section
879 intercomparison (GPCI). *Journal of Climate*, *24*(20), 5223–5256. doi:
880 /10.1175/2011JCLI3672.1
- 881 Thuburn, J., Efstathiou, G. A., & Beare, R. J. (2019). A two-fluid single-column
882 model of the dry, shear-free, convective boundary layer. *Quarterly Journal of
883 the Royal Meteorological Society*, *145*(721), 1535–1550. doi: /10.1002/qj.3510
- 884 Thuburn, J., Weller, H., Vallis, G. K., Beare, R. J., & Whittall, M. (2018). A
885 framework for convection and boundary layer parameterization derived from
886 conditional filtering. *Journal the of the Atmospheric Sciences*, *75*, 965–981.
887 doi: 10.1175/JAS-D-17-0130.1
- 888 Tian, Y., & Kuang, Z. (2016). Dependence of entrainment in shallow cumulus con-
889 vection on vertical velocity and distance to cloud edge. *Geophysical Research
890 Letters*, *43*(8), 4056–4065. doi: 10.1002/2016GL069005
- 891 Turner, J. S. (1963). The motion of buoyant elements in turbulent surroundings.
892 *Journal of Fluid Mechanics.*, *16*, 1–16. doi: 10.1017/S0022112063000549
- 893 Weller, H., & McIntyre, W. A. (2019). Numerical solution of the conditionally
894 averaged equations for representing net mass flux due to convection. *Quar-
895 terly Journal of the Royal Meteorological Society*, *145*(721), 1337–1353. doi:
896 doi.org/10.1002/qj.3490
- 897 Wu, E., Yang, H., Kleissl, J., Suselj, K., & Kurowski, M. (2020). On the parame-
898 terization of convective downdrafts for marine stratocumulus clouds. *Monthly
899 Weather Review*. doi: 10.1175/MWR-D-19-0292.1
- 900 Xie, S., Wang, Y.-C., Lin, W., Ma, H.-Y., Tang, Q., Tang, S., . . . Zhang, M. (2019).
901 Improved diurnal cycle of precipitation in e3sm with a revised convective
902 triggering function. *Journal of Advances in Modeling Earth Systems*, *11*(7),
903 2290–2310. doi: 10.1029/2019MS001702
- 904 Yano, J.-I. (2014). Formulation structure of the mass-flux convection pa-
905 rameterization. *Dynamics of Atmospheres and Oceans*, *67*, 1–28. doi:
906 0.1016/j.dynatmoce.2014.04.002